

Auto-Encoded Supervision for Perceptual Image Super-Resolution

MinKyu Lee, Sangeek Hyun, Woojin Jun, Jae-Pil Heo*
Sungkyukwan University

{2minkyulee, hsi1032, junwoojin, jaepilheo}@skku.edu

Abstract

This work tackles the *fidelity* objective in the *perceptual super-resolution (SR)*. Specifically, we address the shortcomings of pixel-level \mathcal{L}_p loss (\mathcal{L}_{pix}) in the GAN-based SR framework. Since \mathcal{L}_{pix} is known to have a trade-off relationship against perceptual quality, prior methods often multiply a small scale factor or utilize low-pass filters. However, this work shows that these circumventions fail to address the fundamental factor that induces blurring. Accordingly, we focus on two points: 1) precisely discriminating the subcomponent of \mathcal{L}_{pix} that contributes to blurring, and 2) only guiding based on the factor that is free from this trade-off relationship. We show that they can be achieved in a surprisingly simple manner, with an Auto-Encoder (AE) pretrained with \mathcal{L}_{pix} . Accordingly, we propose the Auto-Encoded Supervision for Optimal Penalization loss ($\mathcal{L}_{\text{AESOP}}$), a novel loss function that measures distance in the **AE space**¹, instead of the raw pixel space. By simply substituting \mathcal{L}_{pix} with $\mathcal{L}_{\text{AESOP}}$, we can provide effective reconstruction guidance without compromising perceptual quality. Designed for simplicity, our method enables easy integration into existing SR frameworks. Experimental results verify that AESOP can lead to favorable results in the perceptual SR task.

1. Introduction

Image Super-Resolution is a fundamental challenge in image processing, where the goal is to reconstruct an unknown high-resolution (HR) image from its low-resolution (LR) counterpart. Recent advances in this field have branched into two distinct mainstreams; fidelity-oriented SR and perceptual quality oriented SR (perceptual SR). Fidelity-oriented SR methods aim for high fidelity towards the HR image on a pixel-wise basis. These methods generally adopt the per-pixel reconstruction loss \mathcal{L}_{pix} (i.e., pixel-level \mathcal{L}_p loss), thereby regressing the unique point that minimizes the expected error. This unique point of minimum expected error is known as the average point over multiple plausible solutions [31], which we will refer to as the *optimal fidelity point* (brown dot in Fig.1.(a)) throughout this work. Another

branch of research is the perceptual SR task where the emphasis is on generating visually plausible SR images rather than mere minimum pixel-wise error. Notably, the inherent ill-posedness leads perceptual SR to exhibit a range of variant realistic solutions (multiple purple points in Fig.1.(a)), each pivotal to the aforementioned optimal fidelity point.

Here, the representative framework in perceptual SR is the SRGAN-based [30] framework, which utilizes perceptual quality oriented losses [22, 54] together with \mathcal{L}_{pix} , the *de facto* training scheme. Yet, since these methods rely on \mathcal{L}_{pix} as their fidelity loss term, they cannot avoid the blurring phenomenon as shown in the perception-distortion (PD) trade-off [2]. To address this, they either apply a small coefficient [30, 54] to \mathcal{L}_{pix} or use low-pass filters (LPF) [11, 69] before calculating \mathcal{L}_{pix} . However, we point out that these circumventions result in suboptimal performance, as they misinterpret the implications of \mathcal{L}_{pix} and fail to distinguish between factors that cause blurring and those that do not.

Accordingly, this work revisits \mathcal{L}_{pix} and aims to correctly analyze the implications of it, by introducing two key factors of an SR image: 1) the *perceptual variance* factor, and 2) the *fidelity bias* factor. Here, the perceptual variance is a necessary variance that captures realistic textures and fine details (red line in Fig.1.(a)). Meanwhile, the fidelity bias is the residual component of the SR image, apart from the perceptual variance factor. This can be understood as the blurry average solution without the fine-grained texture that possesses randomness (no variance, Fig.3.(d)), or can also be understood as the centroid of the distribution where the SR image was originally expected to be sampled from (orange dot in Fig.1.(a)). For an optimal SR image (or the HR), the fidelity bias of itself is the optimal fidelity point.

In terms of these two key components defined above, we will show that \mathcal{L}_{pix} is identical to minimizing both the fidelity bias induced errors and the perceptual variance factor. However, while minimizing the fidelity bias induced error is an intended aspect of \mathcal{L}_{pix} , vanishing perceptual variance is not suitable in perceptual SR. Specifically, when the perceptual variance factor is minimized, the prediction space degenerates and the SR image converges to the blurry average image as in Fig.1.(b). Meanwhile, perceptual quality ori-

*Corresponding author.

¹AE space indicates the space *after* the decoder, not the bottleneck.

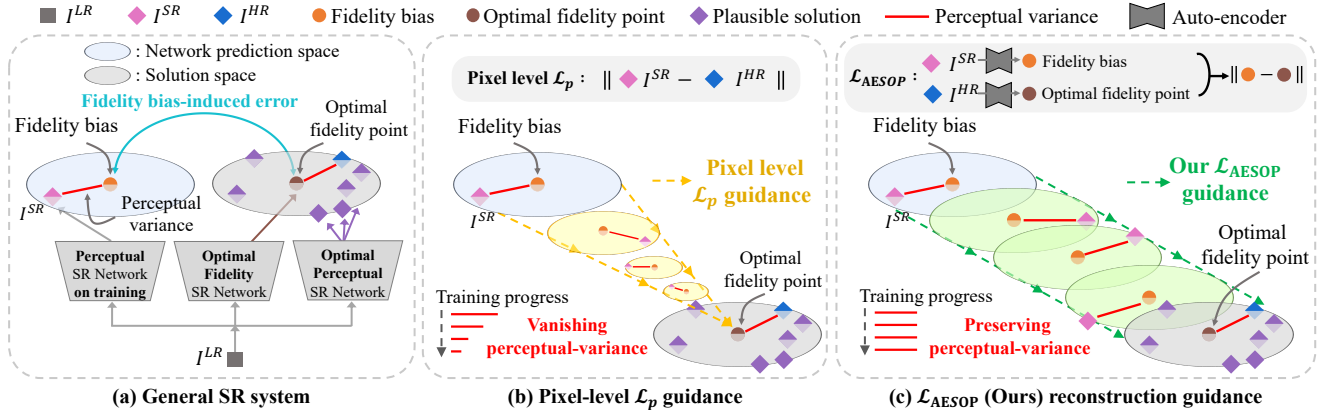


Figure 1. Conceptual illustration of the proposed AESOP loss and the pixel-level \mathcal{L}_p reconstruction guidance employed in typical perceptual SR methods. (a) Fidelity oriented SR network trained with \mathcal{L}_{pix} estimates the average over plausible solutions (i.e., the optimal fidelity point). Meanwhile, perceptual SR involves a range of multiple solutions, standing around the optimal fidelity point. Thus, we identify two fundamental components of a perceptual SR image as 1) the perceptual variance factor (red line), a factor that possesses randomness and contributes to realistic textures, and 2) the fidelity bias term (orange dot), the residual blurry component of an SR image, contributing to the overall fidelity, apart from the perceptual variance. (b) Typical perceptual SR methods adopt \mathcal{L}_{pix} for reconstruction guidance, which pushes the perceptual variance factor to vanish. Thus, when combined with perceptual quality oriented losses that encourage this variance factor, conflict arises, leading to suboptimal performance. (c) In contrast, $\mathcal{L}_{\text{AESOP}}$ only penalizes the fidelity bias-induced error, while preserving these critical perceptual variance factors. This ensures improved fidelity without sacrificing perceptual quality.

ented losses aim to preserve this necessary perceptual variance, which indicates a conflict against \mathcal{L}_{pix} . Consequently, as long as the SR network receives reconstruction guidance from \mathcal{L}_{pix} , the perceptual quality oriented losses cannot converge to an optimal point, limiting the visual quality.

Now, we focus on the other counterpart of the SR image, the fidelity bias, and the error induced by it. The fidelity bias induced error indicates the overall degree of misalignment between the prediction space and the solution space. Accordingly, reducing the fidelity bias induced error is identical to aligning the centroids of the prediction space and the solution space, without altering the range of the prediction space (i.e., preserving perceptual variance), as in Fig.1.(c). Thus, by reducing the fidelity bias induced error, we can achieve improved fidelity without degrading perceptual variance, which is a highly desired aspect for optimal reconstruction guidance in the perspective of perceptual SR.

Accordingly, this motivates us to design a novel reconstruction loss that can precisely discriminate the fidelity bias and the perceptual variance, and solely penalize based on the fidelity bias term. Notably, we will show that this can be surprisingly simplified with a pretrained Auto-Encoder (AE). We will pretrain an AE with \mathcal{L}_{pix} , and take \mathcal{L}_p in the AE space instead of raw pixel space. Since \mathcal{L}_{pix} removes perceptual variances, loss in the AE space will enable us to penalize solely based on fidelity biases. Importantly, we are conversely taking advantage of the vanishing perceptual variance phenomenon of \mathcal{L}_{pix} , which was observed as a critical limitation. We refer to this as the Auto-Encoded Supervision for Perceptual SR (AESOP).

In summary, our contributions can be simplified as fol-

lows. First, we point out the implications of \mathcal{L}_{pix} in the context of the perceptual SR task, which has often been misunderstood. Second, we propose a novel reconstruction loss that only penalizes the fidelity bias factors, thereby preserving visually important perceptual variance factors of SR images. Finally, we provide extensive experiments that validate the effectiveness of AESOP, leading to significant improvement in the perceptual SR task.

Disclaimer. Perceptual oriented losses are responsible for handling the preserved perceptual variance term, thereby generating realistic textures and fine-details. We keep improvements on these losses out of the scope of this work.

2. Related work

Fidelity-oriented SR. The pioneering works [13, 25], CNN-based [9, 16, 39, 45, 47, 68, 70] and Swin Transformer [40] based methods [5, 6, 34, 36, 63] have shown remarkable improvements. The majority of these methods employ \mathcal{L}_{pix} as their sole objective. Thus, they minimize the expected per-pixel distance, which leads them to estimate the average over multiple solutions [20, 41]. This leads to a high PSNR score but is empirically shown to be blurry. In our work, the *optimal fidelity point* is the optimal estimation of these fidelity-oriented SR methods.

Perceptual SR. The emphasis here is on visual quality over mere per-pixel error. These methods [30, 42, 64, 67] commonly adopt the SRGAN [30]-based framework, integrating \mathcal{L}_{pix} with perceptual-quality-oriented losses such as perceptual loss [22] and adversarial loss [15]. This framework aims to enhance visual quality while retaining a fair amount of fidelity to the HR image. Recently, diffusion-based SR

methods [50, 53, 61] have shown significant progress. However, due to their limitations in SR tasks without complex degradations and the high computational cost, GAN-based SR remains as one of the main branches of research [29]. We limit the scope of our work to GAN-based SR methods. **Improvements in the SRGAN-framework.** Advancements were made on the adversarial loss [27, 54], discriminator architecture [33, 48] and the perceptual loss [10, 28, 49], and also in enhancing GAN stability [27, 37, 42, 59]. Despite remarkable improvements, all these efforts primarily concentrate on perceptual-oriented loss factors. Meanwhile, the use of \mathcal{L}_{pix} for perceptual SR tasks has not been thoroughly investigated. To the best of our knowledge, this is the first attempt that successfully tackles the *fidelity*-loss in a *perceptual* SR framework, removing the problematic pixel-level reconstruction loss in the SRGAN-framework.

3. Revisiting per-pixel loss in perceptual SR

Considering the Oracle case. Consider an optimal perceptual SR network that can sample images from the true posterior. By construction, SR images generated from this network are valid solutions but are not necessarily a pixel-wise exact match to the specific HR image instance in our dataset, due to the inherent ill-posed nature of SR. Yet, \mathcal{L}_{pix} compares two images on a strict pixel-wise basis. This results in penalizing the SR image, despite it being an ideal solution in the context of perceptual SR, by construction.

Revisiting \mathcal{L}_{pix} in perceptual SR. The phenomenon where even an optimal network gets penalized under \mathcal{L}_{pix} results in blurred texture. This is grounded in the fact that training with \mathcal{L}_{pix} is effectively a Maximum Likelihood Estimation, which jointly minimizes both bias errors and also *variance in predictions*. Specifically, prior works [21, 32] have shown that this can be decomposed into jointly minimizing two terms: the systematic-effect (SE) term and the variance-effect (VE) term, which are induced by the bias and variance of the prediction, respectively. Formally, given a symmetric loss function \mathcal{L} and $y \sim p(y|x)$ for an input x , the training objective $\min_{\hat{y}} \mathbb{E}_{y, \hat{y}}[\mathcal{L}(y, \hat{y})]$ can be simplified² as:

$$\min_{\hat{y}} \left\{ \underbrace{\mathbb{E}_y[\mathcal{L}(y, \mu_{\hat{y}}) - \mathcal{L}(y, \mu_y)]}_{\text{SE}(y, \hat{y}): \text{LF + regressable HF}} + \underbrace{\mathbb{E}_{y, \hat{y}}[\mathcal{L}(y, \hat{y}) - \mathcal{L}(y, \mu_{\hat{y}})]}_{\text{VE}(y, \hat{y}): \text{non-regressable HF}} \right\}, \quad (1)$$

with \hat{y} as an estimator of y , and $\mu_y = \arg \min_{\mu} \mathbb{E}_y[\mathcal{L}(y, \mu)]$ and $\mu_{\hat{y}} = \arg \min_{\mu} \mathbb{E}_{y, \hat{y}}[\mathcal{L}(\hat{y}, \mu)]$. With Gaussian prior on \mathcal{L} , the two terms above are further simplified as follows:

$$\begin{aligned} \text{SE}(y, \hat{y}) &= \mathbb{E}_y[(y - \mu_{\hat{y}})^2 - (y - \mu_y)^2] = (\mu_{\hat{y}} - \mu_y)^2 \\ \text{VE}(y, \hat{y}) &= \mathbb{E}_{y, \hat{y}}[(y - \hat{y})^2 - (y - \mu_{\hat{y}})^2] = \mathbb{E}_{\hat{y}}[(\hat{y} - \mu_{\hat{y}})^2]. \end{aligned} \quad (2)$$

SE and VE in terms of perceptual SR. For the perceptual SR task, SE minimization is desired but VE should be

²The irreducible variance term of y is omitted here.

sufficiently preserved. We elaborate on the details below.

VE refers to the additional error introduced by generating components with inherent randomness. In perceptual SR, this is a necessary and inevitable error term induced by fine-grained textures, which cannot be learned via regression. Accordingly, we define the VE term as the *perceptual variance* factor. Here, minimizing VE can be understood as further reducing the expected pixel-wise error, apart from reducing SE, at the cost of removing visually important fine textures. In other words, VE is the factor that leads to the PD trade-off due to its randomness, and VE minimization pushes the prediction space to degenerate, only accepting the average solution as in Fig.1.(b), which is blurry [30].

Focusing now on SE, this is an *unnecessary error term* that can be reduced without inducing PD trade-off since it does not have randomness. Intuitively, it is the overall degree of alignment between the SR and HR image. More specifically, this is the distance between the centroids of the two distributions, where the HR and SR images are each expected to be sampled from. Since these centroids are the minimum expected error points of each distribution, they resemble the fidelity-oriented SR counterpart of the perceptual SR images [31], as in Fig.1.(a). Accordingly, we define each factor in the SE term ($\mu_y, \mu_{\hat{y}}$) as the *fidelity biases*, and SE itself as the fidelity bias induced error. Note that fidelity biases are not simply low-frequency (LF) components. As often reflected in fidelity-oriented SR methods, specific HF components such as simple object boundaries and edges can be learned via pixel-level regression. Fidelity biases include these regressable high-frequency components.

Overall, since VE is the sole factor inducing the PD trade-off, it is straightforward that we can safely reduce SE without harming perception. By minimizing SE for a given VE, we can obtain the maximum fidelity for a given perception level; the ideal PD trade-off³. At the same time, a sufficient level of VE should be preserved for visual quality. Accordingly, the following sections will elaborate on designing a novel loss that minimizes SE while preserving VE, taking a step toward the optimal perceptual SR network.

Revisiting prior methods. Observations above share some key concepts with the well-known perception-distortion (PD) trade-off [2]. However, we highlight aspects of \mathcal{L}_{pix} that are often overlooked in most training methods, with the terms defined above. Specifically, previous approaches aim to avoid blurring by either 1) introducing LPF before loss calculation [11, 69] or 2) simply applying a small coefficient for \mathcal{L}_{pix} [30, 37, 54]. Below, we will show that both are misinterpreting the blurring phenomenon.

First, LPF-based approaches remove more information than required. They assume that the fidelity biases solely consist low-frequency image components. Yet, bias fac-

³Note that zero SE alone does not indicate optimal *perception*.

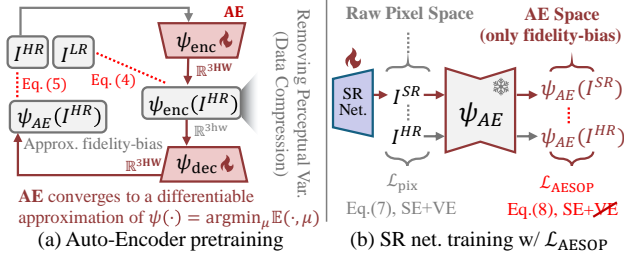


Figure 2. (a) We pretrain an Auto-Encoder ψ_{AE} that removes perceptual variance factors, thereby establishing a feature space where only the fidelity bias factors reside. (b) The main SR network training step with the proposed \mathcal{L}_{AESOP} . By applying reconstruction objectives such as the \mathcal{L}_1 loss in the auto-encoded space, we can solely target the fidelity bias induced error without suffering from vanishing perceptual variance (i.e., suffer from blurring). We omit perceptual-quality-oriented losses here.

tors $(\mu_y, \mu_{\hat{y}})$ include certain high-frequency components as discussed above. Therefore, despite that LPF-based approaches can avoid texture blurring induced by VE, they also fail to guide regressable high-frequency components that are free from texture blurring. By not providing guidance for certain components of SE, they achieve lower fidelity than necessary, failing to reach the optimal PD trade-off. We provide further analysis for this in Sec.5.2.

Meanwhile, applying a small coefficient to \mathcal{L}_{pix} misguidedly treats all aspects of \mathcal{L}_{pix} as contributing to blurring. This indiscriminative approach unintentionally weakens SE reduction. When combined with the adversarial loss, this also leads to redundant SE, failing to reach the optimal PD trade-off. This is because adversarial loss works in a task-blind, unsupervised manner: it improves realism but does not consider the alignment between the input image and the network output. As this significantly hinders SE convergence [37, 59], strong guidance on the SE factor is required to prevent high SE. However, the small coefficient greatly reduces this guidance, resulting in unnecessary fidelity loss and a suboptimal PD trade-off. Additionally, since \mathcal{L}_{pix} fundamentally enforces VE reduction, it can also never achieve optimal perception despite applying a small scale factor. See Appendix.F for discussions and graphical illustrations.

4. Method

Motivation. An optimal perceptual SR should minimize fidelity bias induced errors while preserving perceptual variance. However, prior methods often fail to achieve this due to their inability to effectively discriminate these factors. This motivates us to design a new method that disentangles them, and solely penalizes based on fidelity biases, bringing us closer to the optimal perceptual SR.

Overview. The proposed method can be simplified into two steps. First, we develop an Auto-Encoder (AE), tailored to create a feature space exclusively for fidelity biases. Second, instead of taking \mathcal{L}_p in raw pixel space as typical

methods, we calculate \mathcal{L}_p in the AE space as in Fig.2. Taking \mathcal{L}_p in the AE space enables us to provide effective reconstruction guidance with preserved perceptual variance. Note that the term *AE space* indicates the space after the decoder, not the bottleneck. Fundamentally, we are utilizing an AE as a differentiable approximation of an operator $\psi(\cdot) := \arg \min_{\mu} \mathbb{E}[\mathcal{L}(\cdot, \mu)]$ to substitute \mathcal{L}_{pix} with SE.

Baseline. This work aims to make improvements in the GAN-based perceptual SR task. Accordingly, we follow a recent GAN-based SR method LDL [37], and set our baseline training objective as below:

$$\mathcal{L}_{base} = \lambda_1 \mathcal{L}_{pix} + \lambda_2 \mathcal{L}_{percep} + \lambda_3 \mathcal{L}_{adv} + \lambda_4 \mathcal{L}_{artif}, \quad (3)$$

where \mathcal{L}_{pix} , \mathcal{L}_{percep} , \mathcal{L}_{adv} , \mathcal{L}_{artif} are the widely used pixel-level \mathcal{L}_p loss, perceptual loss [22], the adversarial loss [54], and the artifact loss [37], respectively, and $\lambda_1, \lambda_2, \lambda_3, \lambda_4$ are coefficients for each loss factors, respectively. We limit the scope of this work to tackling the *fidelity* loss term of *perceptual* SR, thus, we will only modify \mathcal{L}_{pix} , while leaving all other loss terms unchanged.

4.1. Auto-Encoder pretraining

Designing the fidelity bias feature space. Our aim is to provide reconstruction supervision focused exclusively on SE. Given that the only components of SE are the fidelity biases $(\mu_y, \mu_{\hat{y}})$, our task simplifies into estimating an operator ψ that estimates the fidelity bias of a given image as $\psi(\cdot) := \arg \min_{\mu} \mathbb{E}[\mathcal{L}(\cdot, \mu)]$. To maintain simplicity, we employ a basic Auto-Encoder (AE) to construct a differentiable approximation of this operator. This architectural choice is grounded by the nature of SR, where the HR images are conditioned by the LR images and the scale factor. Thus, we model this relationship as $y \sim p(y|x) = p(y|\phi(y, s))$, where x is the observed LR image, ϕ is the $\times s$ downsampling function. In essence, HR images are derived from a distribution conditioned on themselves and the scale factor s . Additionally, the definition of ψ involves minimizing the expected loss over this conditional distribution. Thus, our method is followed by pretraining the AE to reconstruct the input with the \mathcal{L}_p loss. Accordingly, the pretrained AE will act as a differentiable approximation of ψ , which can decompose the fidelity bias of images and can also be directly plugged into the training framework.

To provide further intuition, we emphasize that the bottleneck of our AE is designed to have the same dimensionality as the LR image. Contrary to most AEs or feature encoders [22], which use a high-dimensional latent space to learn *additional semantics or high-level representations* beyond the raw pixel space, our AE is specifically designed to *remove* particular *low-level* features from the pixel space. The carefully chosen architecture and pretraining objective form an information bottleneck that effectively compresses out factors that have inherent randomness. Since this is the

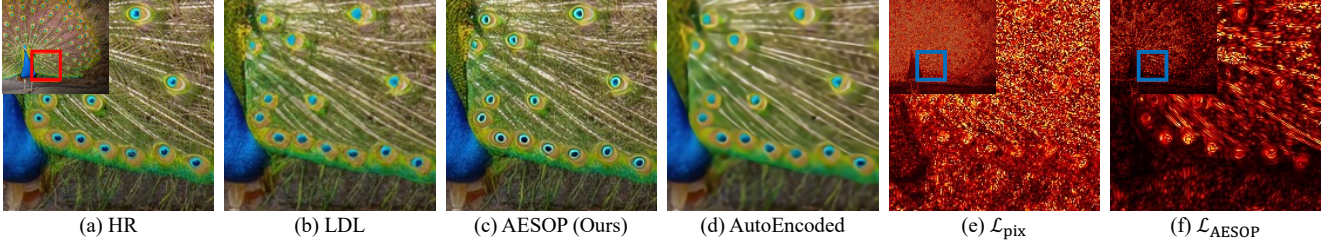


Figure 3. Key components of $\mathcal{L}_{\text{AESOP}}$ and \mathcal{L}_{pix} on SwinIR-backbone. \mathcal{L}_{pix} in (e) penalizes perceptually-variance factors, leading to blurry images in (b). In contrast, $\mathcal{L}_{\text{AESOP}}$ in (f) only penalizes based the fidelity bias (d), which enables us to obtain increased realism as in (c).

perceptual variance, we can isolate only the fidelity bias as in Fig.2. Thus, \mathcal{L}_p in the AE space resembles loss between fidelity biases, which is fundamentally identical to SE: a term that improves fidelity without inducing blurring. Notably, while vanishing perceptual variance was observed as a critical limitation of \mathcal{L}_{pix} in the perceptual SR task, we are conversely taking advantage of it by removing perceptual variance factors in our newly designed fidelity loss term.

AE pretraining. To design a fidelity bias estimator, we pre-train our AE to approximate $\psi(\cdot) := \arg \min_{\mu} \mathbb{E}[\mathcal{L}(\cdot, \mu)]$ for $y \sim p(y|x) = p(y|\phi(y, s))$. Thus, the AE is pretrained to condition itself by estimating $\phi(y, s)$ and then reconstructs y . That is, it learns to consecutively estimate the LR and HR image by minimizing \mathcal{L}_p for each as follows:

$$\mathcal{L}_{\text{LR}}^{\text{rec}} = \|\psi_{\text{enc}}(I^{\text{HR}}) - I^{\text{LR}}\|_p \quad (4)$$

$$\mathcal{L}_{\text{HR}}^{\text{rec}} = \|\psi_{\text{AE}}(I^{\text{HR}}) - I^{\text{HR}}\|_p, \quad (5)$$

where $\psi_{\text{AE}} := \psi_{\text{dec}} \cdot \psi_{\text{enc}}$ denotes the AE, $\psi_{\text{enc}}, \psi_{\text{dec}}$ is the encoder and decoder, and $I^{\text{LR}}, I^{\text{HR}}$ are LR, HR images. The AE will act as an effective bias estimator, enabling us to design a space where only fidelity biases reside. Note that these losses are only used to pretrain the AE, and will not be used when training the SR network.

AE architecture. Based on the constructions above, the encoder takes an HR image, and estimates the corresponding LR versions; and the decoder, vice-versa as follows:

$$\psi_{\text{enc}} := \mathbb{R}^{3\text{HW}} \mapsto \mathbb{R}^{3\text{hw}}, \quad \psi_{\text{dec}} := \mathbb{R}^{3\text{hw}} \mapsto \mathbb{R}^{3\text{HW}}, \quad (6)$$

where HW and hw each indicate the spatial dimension of the HR and LR images. Since the decoding process resembles a fidelity oriented SR task, we employ an off-the-shelf SR architecture RRDBNet [54], and initialize the decoder as the pretrained weights for the fidelity-oriented SR task. The encoder is simply a lightweight CNN with downsampling. Refer to the appendix for further details.

Bottleneck collapse. Consider a scenario where the encoder exactly matches the corresponding LR image of the input. If the SR image simply downscales to the original LR image, no loss would backpropagate regardless of the regressable high-frequency component quality of the SR image. Since this can potentially harm the performance, the encoder is jointly optimized with the decoder for Eq.(5).

4.2. Auto-Encoded supervision

Defining the AESOP loss. Since we have obtained a feature space that only retains the fidelity bias factors, we finally define $\mathcal{L}_{\text{AESOP}}$ as \mathcal{L}_p with auto-encoded versions of HR and SR images. Contrary to \mathcal{L}_{pix} which minimizes both SE and VE, the proposed $\mathcal{L}_{\text{AESOP}}$ only minimizes SE is as follows:

$$\mathcal{L}_{\text{pix}} = \|I^{\text{HR}} - I^{\text{SR}}\|_p \quad (= \text{SE} + \text{VE}), \quad (7)$$

$$\mathcal{L}_{\text{AESOP}} = \|\psi_{\text{AE}}(I^{\text{HR}}) - \psi_{\text{AE}}(I^{\text{SR}})\|_p \quad (\approx \text{SE} + \mathcal{Y}\mathcal{E}), \quad (8)$$

where $I^{\text{HR}}, I^{\text{SR}}$ represent HR, SR images, respectively. Considering the AE pretraining, ψ_{AE} is a differential approximation of a fidelity bias estimator. Thus, $\mathcal{L}_{\text{AESOP}}$ is now fundamentally identical to only penalizing the SE factor of Eq.(2) or Eq.(7). Since these features are decoupled from the perceptual variance factors by construction, $\mathcal{L}_{\text{AESOP}}$ leads to increased fidelity without forcing visually important textures to vanish. Also, note that *auto-encoded* indicates the space after the decoder, not the bottleneck.

Final objective function. Since we focus on improving the *fidelity* loss term of the framework, we substitute \mathcal{L}_{pix} with $\mathcal{L}_{\text{AESOP}}$, leading to the overall objective function as follows:

$$\mathcal{L}_{\text{total}} = \lambda_{\text{AESOP}} \mathcal{L}_{\text{AESOP}} + \lambda_2 \mathcal{L}_{\text{percep}} + \lambda_3 \mathcal{L}_{\text{artif}} + \lambda_4 \mathcal{L}_{\text{adv}}, \quad (9)$$

where $\lambda_{\text{AESOP}}, \lambda_2, \lambda_3, \lambda_4$ are coefficients for each loss factors. The overall pipeline of our training strategy is visualized in Fig.2. Based on the constructions above, the proposed $\mathcal{L}_{\text{AESOP}}$ provides reconstruction guidance without facing conflicts with the perceptual-quality-oriented losses. This indicates that both the $\mathcal{L}_{\text{AESOP}}$ and perceptual-quality-oriented losses can converge to an optimal point, leading to increased performance in terms of perception-distortion trade-off [2]. Accordingly, while typical methods multiply a very small coefficient to the reconstruction loss (generally chosen as 0.01 [37, 54]) to prevent blurring effects, we let $\lambda_{\text{AESOP}} = 1$. This way, we can provide significantly stronger reconstruction guidance without suffering from unintended blurring, leading to both lower levels of artifacts [37] and enhanced realism. For the other coefficients, we follow our baseline [37] settings and choose $\lambda_2 = 1, \lambda_3 = 1, \lambda_4 = 0.005$.

AE collapse. Eq.(8) leads to a trivial solution when the AE outputs the same value regardless of the input. To prevent this, we keep the AE frozen when training the SR network.

Backbone		RRDB					SwinIR			
Metrics	Benchmark	ESRGAN	SPSR	LDL	AESOP	AESOP [†]	+GAN	LDL	AESOP*	AESOP
Recon. Objective		\mathcal{L}_{pix}	\mathcal{L}_{pix}	\mathcal{L}_{pix}	$\mathcal{L}_{\text{AESOP}}$	$\mathcal{L}_{\text{AESOP}}$	\mathcal{L}_{pix}	\mathcal{L}_{pix}	$\mathcal{L}_{\text{AESOP}}$	$\mathcal{L}_{\text{AESOP}}$
Patch Size (Training)		128	128	128	128	256	256	256	256	256
LPIPS ↓	Set14	0.1241	0.1207	0.1132	0.1067	0.1053	0.1160	0.1091	0.1023	0.1027
	Manga109	0.0649	0.0672	0.0544	0.0525	0.0494	0.0542	0.0469	0.0440	0.0461
	General100	0.0879	0.0862	0.0796	0.0784	0.0734	0.0796	0.0740	0.0717	0.0710
	Urban100	0.1229	0.1184	0.1084	0.1064	0.1033	0.1077	0.1021	0.0961	0.0945
	DIV2K-val	0.1154	0.1099	0.0999	0.0977	0.0936	0.1038	0.0944	0.0909	0.0893
	BSD100	0.1616	0.1609	0.1535	0.1515	0.1443	-	0.1572	0.1441	0.1385
	LSDIR	0.1378	0.1312	0.1180	0.1152	0.1123	-	0.1132	0.1094	0.1071
DISTS ↓	Set14	0.0951	0.0920	0.0866	0.0852	0.0825	0.0930	0.0869	0.0809	0.0819
	Manga109	0.0471	0.0463	0.0355	0.0360	0.0356	0.0365	0.0315	0.0327	0.0328
	General100	0.0874	0.0884	0.0801	0.0798	0.0773	0.0835	0.0794	0.0768	0.0762
	Urban100	0.0880	0.0849	0.0793	0.0793	0.0768	0.0835	0.0800	0.0751	0.0742
	DIV2K-val	0.0593	0.0546	0.0526	0.0518	0.0484	0.0531	0.0507	0.0469	0.0459
	BSD100	0.1165	0.1176	0.1163	0.1117	0.1089	-	0.1185	0.1078	0.1072
	LSDIR	0.0764	0.0699	0.0650	0.0641	0.0612	-	0.0650	0.0601	0.0591
PSNR ↑	Set14	26.594	26.860	27.228	27.361	27.246	27.282	27.526	27.822	27.421
	Manga109	28.413	28.561	29.620	29.973	29.747	29.345	30.143	30.453	30.061
	General100	29.425	29.424	30.289	30.482	30.251	30.104	30.441	30.752	30.401
	Urban100	24.365	24.804	25.459	25.630	25.541	25.736	26.231	26.398	26.148
	DIV2K-val	28.175	28.182	28.819	29.079	28.910	28.784	29.117	29.543	29.137
	BSD100	25.313	25.501	25.954	26.080	25.904	-	26.216	26.405	25.930
	LSDIR	23.882	24.232	24.663	24.933	24.845	-	25.129	25.419	25.038
SSIM ↑	Set14	0.7144	0.7254	0.7358	0.7402	0.7371	0.7407	0.7478	0.7578	0.7438
	Manga109	0.8595	0.8590	0.8734	0.8827	0.8802	0.8796	0.8880	0.8949	0.8880
	General100	0.8095	0.8091	0.8280	0.8335	0.8269	0.8305	0.8347	0.8415	0.8328
	Urban100	0.7341	0.7474	0.7661	0.7724	0.7697	0.7786	0.7918	0.7947	0.7884
	DIV2K-val	0.7759	0.7720	0.7897	0.7978	0.7951	0.7911	0.8011	0.8121	0.8023
	BSD100	0.6527	0.6596	0.6813	0.6841	0.6783	-	0.6923	0.6982	0.6813
	LSDIR	0.6866	0.6966	0.7117	0.7220	0.7202	-	0.7316	0.7397	0.7289

Table 1. Quantitative comparison between AESOP (Ours) and baseline methods. The best results of each group are highlighted in **bold**. AESOP* indicates only training 200K iterations, AESOP[†] indicates training with a larger patch.

5. Experiments

5.1. Benchmark evaluation

Experimental setup. We employ benchmark datasets including Set14 [62], Manga109 [44], General100 [14], Urban100 [19], DIV2K [1], BSD100 [43], LSDIR [35]. For both the AE pretraining and the SR network training, we use DF2K, a combination of DIV2K [1] and Flickr2K [38]. We report PSNR and SSIM [57] scores for distortion metrics and LPIPS [66], DISTS [12] for perceptual quality metrics. We use both RRDB-based models: ESRGAN [54], SPSR [42], LDL [37], CALGAN[48]; and SwinIR-based versions of each, if available. AESOP is used interchangeably to indicate either $\mathcal{L}_{\text{AESOP}}$ or the SR networks trained with Eq.(9). Refer to the Appendix for details on experimental settings.

Quantitative comparison. In Tab. 1, we perform a quantitative evaluation against baseline GAN-based perceptual SR methods. Against all RRDB [54] based baseline methods, AESOP significantly improves both distortion metrics and perceptual scores. We find the key factor of this improvement as the carefully designed feature space and pretrained AE. It provides an increased level of reconstruction guidance, specifically to fidelity bias factor, while providing additional freedom to perceptual-quality-oriented losses. For

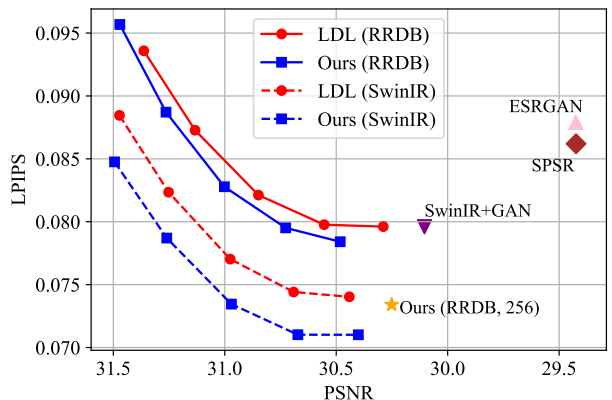
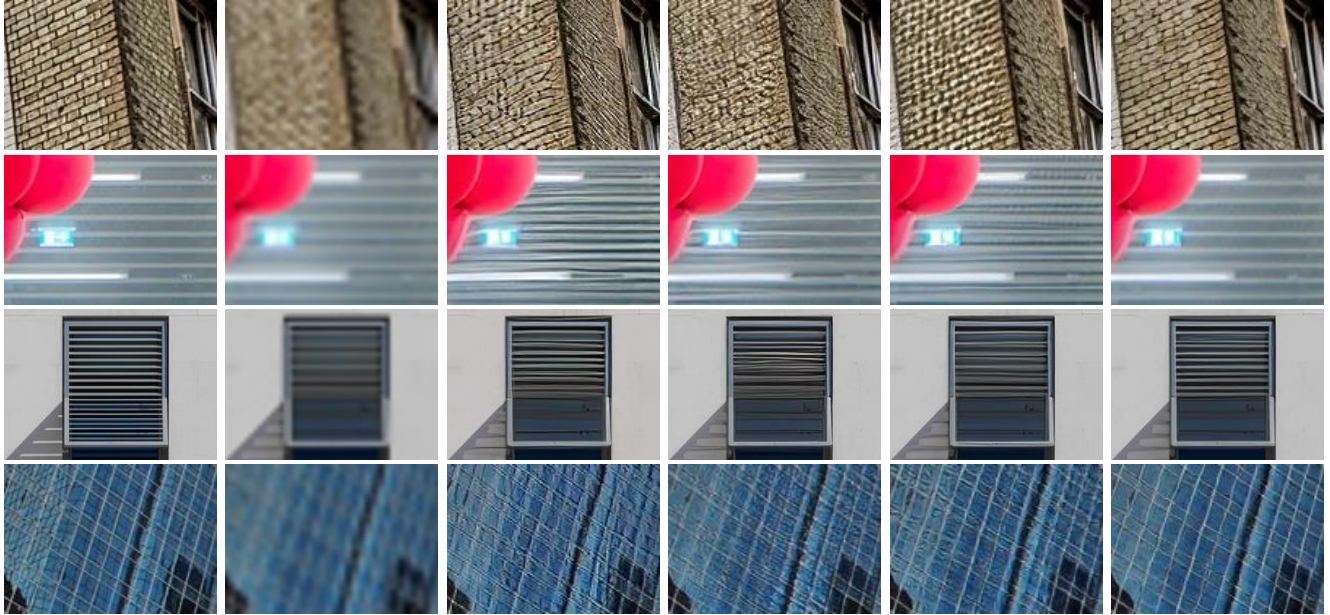


Figure 4. The PD trade-off curve. The backbone and training patch size are indicated; if not specified, the default patch size is 128.

SwinIR [36] backbone methods, we report both the final results at 300K iterations and intermediate training results at 200K iterations (indicated as AESOP*). At 200K, it can be seen that AESOP leads to improvements in both fidelity scores and perceptual metrics, similar to the RRDB-backbone. When we fully train our model up to 300K, we observe further enhancements in perception scores. Since improved perception leads to lower fidelity due to the PD trade-off, we provide the PD trade-off curves in Fig.4, with



(a) HR (b) Bicubic (c) ESRGAN (d) SPSR (e) LDL (f) AESOP (Ours)

Figure 5. Visual comparison of AESOP with baseline methods for the $\times 4$ SR task on the RRDB backbone. Our method produces images with fewer visual artifacts. See the Appendix for more visual examples of AESOP’s improvement in realism and fine details.

PSNR and LPIPS scores on the General100 dataset. AESOP leads to improved trade-off relationships on both RRDB and SwinIR backbones. Additionally, we provide RRDB-backbone results using a training HR patch size of 256 (denoted as AESOP[†]) to align with the training settings of SwinIR. AESOP also improves realism for real-world SR tasks as in Tab.2. Refer to Appendix.B for more results.

Qualitative comparison. In Fig.5, baseline methods often suffer from unpleasant GAN artifacts [37] while AESOP presents a significantly lower level of these artifacts. This is due to the strong reconstruction guidance $\mathcal{L}_{\text{AESOP}}$ provides, since it does not require a small scaling factor. Additionally, refer to the Appendix for visual examples of AESOP improving realism on fine details and complex textures.

Ablation studies. To verify the effects of each component, we perform ablation studies on AESOP (128). In Tab.3, we report DISTS and PSNR scores for each setting on DIV2K validation set. The first line indicates the baseline setting that matches LDL, where none of our proposed components are applied. Tab.3.(a) indicates employing a decoder, but using a simple bicubic downsampling operation instead of the encoder. As reported, the perceptual quality and fidelity are improved even when solely utilizing the decoder due to its ability in offering stronger reconstruction loss without conflict with perceptual objectives. However, the usage of bicubic downsampling with a decoder corresponds to the bottleneck collapse, where no loss backpropagates if the SR image downsamples to the LR image, thus, leading to slightly lower performance against our full method. In Tab.3.(b), we further introduce a learnable encoder to-

Dataset	Method	Recon. Obj.	NIQE \downarrow	MANIQA \uparrow
RealSRv3 [3]	Real-ESRGAN	\mathcal{L}_{pix}	4.6790	0.3662
	AESOP (Ours)	$\mathcal{L}_{\text{AESOP}}$	4.2337	0.4136
DRealSR [58]	Real-ESRGAN	\mathcal{L}_{pix}	4.7152	0.3404
	AESOP (Ours)	$\mathcal{L}_{\text{AESOP}}$	4.1922	0.3917

Table 2. Quantitative results of AESOP in real-world settings. Refer to the Appendix for further results, including visual examples.

	Decoder	Encoder	$\mathcal{L}_{\text{LR}}^{\text{rec}}$	DISTS \downarrow	PSNR \uparrow
Baseline (LDL)				0.0526	28.819
Config-(a)	✓			0.0521	29.060
Config-(b)	✓	✓		0.0526	29.150
Config-(c) (Ours)	✓	✓	✓	0.0518	29.079

Table 3. Ablation study on each component of AESOP (128).

gether with the decoder, but without Eq.(4) (i.e., without estimating the LR image). Given that both fidelity bias factors and perceptual variance factors are determined by the LR counterpart, the model cannot properly estimate the fidelity bias and the perceptual variance. Consequently, the perceptual variance factor can be penalized, which is not intended, leading to the lowest perceptual score. Our full model in Tab.3.(c) further employs Eq.(4). Thus, it better models the LR than Tab.3.(b), while also avoiding the bottleneck collapse which Tab.3.(a) has suffered, leading to the best scores in terms of perceptual quality.

5.2. Analysis

Spectral analysis. Several prior works [11, 69] employ low-pass filtering (LPF) to avoid the blurring effect of \mathcal{L}_{pix} . To identify the difference between our AE and LPF, we analyze the spectral magnitudes of Fig.6.(a) after applying AE

and LPF, in Fig.6.(c)-(d), respectively. As can be seen, LPF blindly removes all HF components, contrary to AE, where certain patterns in the HF regions are preserved. As discussed in Sec. 3, the remaining HF components in Fig.6.(c) are factors that can be learned by pixel-level regression, and the removed HF components are the non-regressable factors (VE) that lead to blurring when minimized.

Here, we focus on the *remaining* HF components and visualize it in Fig.6.(e), by taking the absolute difference between Fig.6.(c)-(d). Simple object edges are highlighted, which are regions where even fidelity-oriented SR networks (trained with pixel-level regression loss, \mathcal{L}_{pix}), can also sharply reconstruct. This indicates that specific HF components *can* be regressed, and importantly, these HF components *cannot* be disentangled from other HF components by band-pass filters (e.g., LPF) or frequency selection [7, 8]; since they are intertwined within the same frequency band.

Meanwhile, LPF is expected to provide limited super-resolution in these regressable HF components, leading to degraded performance. To validate this statement, we compare AESOP against LPF in Tab.5.(b). We apply LPF on SR and HR images before calculating \mathcal{L}_{pix} on top of our baseline method LDL. A notable degradation in performance can be observed, highlighting the superiority of our AE-based method in maintaining high-quality reconstruction guidance over conventional frequency-based methods.

Overall, we conclude that our AE can successfully disentangle fidelity biases and perceptual variances, by capturing specific HF components that 1) cannot be obtained by simple frequency selection, 2) but can be learned via regression, and 3) significantly contribute to improved fidelity.

Loss map comparison. Fig.3 visualizes key components of $\mathcal{L}_{\text{AESOP}}$ and \mathcal{L}_{pix} . In Fig.3.(e), \mathcal{L}_{pix} cannot distinguish perceptual variance factors and fidelity bias factors. Thus, visually important fine-textures are penalized, leading to a blurry result as in Fig.3.(b). Meanwhile, $\mathcal{L}_{\text{AESOP}}$ in Fig.3.(f) successfully extracts and penalizes only the fidelity bias factor Fig.3.(d), leading to increased realism as in Fig.3.(c).

Fidelity bias estimation. Since $\mathcal{L}_{\text{AESOP}}$ does not lead to blurring, we do not multiply a small scaling factor. Accordingly, we can provide significantly stronger guidance on fidelity biases. Here, we measure how well each network estimates the fidelity biases, apart from PSNR scores which are influenced by perceptual variances. To do this, we introduce *AE-PSNR*, which measures the PSNR between auto-encoded SR and HR images. This score reflects how well an image captures the fidelity bias of the reference image. However, since AESOP is trained using the AE, there may be unintended biases introduced by the AE itself. Thus, we additionally report LR-PSNR as an unbiased metric independent of the AE, which measures the PSNR between downsampled SR and the original LR images. This captures

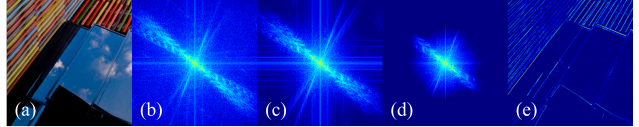


Figure 6. Visual comparison between AE and LPF. (a) Original image. (b) Original image in spectral domain. (c) Forwarding through AE. (d) Applying LPF. (e) Absolute difference between (c) and (d). (Electronic viewer highly recommended.)

	Method	Set14	Mg109	Gen100	Urb100	DIV2K	B100	LSDIR
AE-	LDL [37]	31.525	33.215	33.994	29.374	32.855	29.792	29.071
	Ours	32.111	33.635	34.535	29.666	33.490	30.366	29.552
LR-	LDL [37]	46.899	49.135	48.663	47.404	48.084	45.494	45.731
	Ours	48.245	50.042	49.733	48.564	49.856	47.578	47.476

Table 4. AE-PSNR and LR-PSNR scores with SwinIR-backbone.

	Manga109	General100	Urban100	DIV2K100
Ours	29.97/.0525	30.48/.0784	25.63/.1064	29.08/.0977
(a)	29.78/.0534	30.35/.0789	25.55/.1054	28.97/.0982
LDL	29.62/.0544	30.29/.0796	25.46/.1084	28.82/.0999
(b)	29.55/.0545	30.20/.0801	25.39/.1090	28.75/.1005

Table 5. PSNR/LPIPS scores. (a) AESOP with SRResNet-based AE (ψ). (b) Applying LPF before calculating \mathcal{L}_{pix} with LDL [37].

how well the fidelity biases align, but without being influenced by the AE. However, note that this measure only reflects the LF feature, a subcomponent of the fidelity bias. In Tab.4, AESOP shows improvements on both AE-PSNR and LR-PSNR scores, demonstrating the superiority of $\mathcal{L}_{\text{AESOP}}$ against scaled \mathcal{L}_{pix} in effectively reducing the SE term. See the Appendix for scores on RRDB-backbone methods.

Architectural choice of AE. Performance of AESOP with SRResNet-based [30] AE is reported in Tab.5.(a). We observe a slight performance drop against our RRDB-based AE, but it is still superior against LDL. While this indicates that AESOP relies on a well-performing AE, this reliance does not pose a practical issue. In our pretraining framework, we initialize the decoder of AE as the fidelity-oriented SR network, which is expected to be already in place under the SRGAN-based training framework.

6. Conclusion

This work analyzes limitations of \mathcal{L}_{pix} (i.e., the conventional pixel-level \mathcal{L}_p) in the context of perceptual SR. Further, we highlight the shortcomings of prior circumvention to avoid blurring, in terms of fidelity biases and perceptual variance factors. We tackle this issue by introducing $\mathcal{L}_{\text{AESOP}}$, a novel reconstruction loss that separates fidelity bias factors from perceptual variance factors using an AE, pretrained for a reconstruction task. This allows us to focus on enhancing fidelity while preserving the visual quality of SR images. Experimental results validate that the proposed method leads to significant improvement in the perceptual SR task.

References

- [1] Eirikur Agustsson and Radu Timofte. Ntire 2017 challenge on single image super-resolution: Dataset and study. In *Proceedings of the IEEE Conference on Computer Vision and Pattern Recognition Workshops*, pages 126–135, 2017. 6
- [2] Yochai Blau and Tomer Michaeli. The perception-distortion tradeoff. In *Proceedings of the IEEE conference on computer vision and pattern recognition*, pages 6228–6237, 2018. 1, 3, 5, 7, 8
- [3] Jianrui Cai, Hui Zeng, Hongwei Yong, Zisheng Cao, and Lei Zhang. Toward real-world single image super-resolution: A new benchmark and a new model. In *Proceedings of the IEEE/CVF International Conference on Computer Vision*, pages 3086–3095, 2019. 7, 2
- [4] Lucy Chai, Michael Gharbi, Eli Shechtman, Phillip Isola, and Richard Zhang. Any-resolution training for high-resolution image synthesis. In *European Conference on Computer Vision*, pages 170–188. Springer, 2022. 3
- [5] Hanting Chen, Yunhe Wang, Tianyu Guo, Chang Xu, Yiping Deng, Zhenhua Liu, Siwei Ma, Chunjing Xu, Chao Xu, and Wen Gao. Pre-trained image processing transformer. In *Proceedings of the IEEE/CVF conference on computer vision and pattern recognition*, pages 12299–12310, 2021. 2
- [6] Xiangyu Chen, Xintao Wang, Jiantao Zhou, Yu Qiao, and Chao Dong. Activating more pixels in image super-resolution transformer. In *Proceedings of the IEEE/CVF Conference on Computer Vision and Pattern Recognition*, pages 22367–22377, 2023. 2
- [7] Sung-Jin Cho, Seo-Won Ji, Jun-Pyo Hong, Seung-Won Jung, and Sung-Jea Ko. Rethinking coarse-to-fine approach in single image deblurring. In *Proceedings of the IEEE/CVF international conference on computer vision*, pages 4641–4650, 2021. 8
- [8] Yuning Cui, Yi Tao, Zhenshan Bing, Wenqi Ren, Xinwei Gao, Xiaochun Cao, Kai Huang, and Alois Knoll. Selective frequency network for image restoration. In *The Eleventh International Conference on Learning Representations*, 2023. 8
- [9] Tao Dai, Jianrui Cai, Yongbing Zhang, Shu-Tao Xia, and Lei Zhang. Second-order attention network for single image super-resolution. In *Proceedings of the IEEE/CVF conference on computer vision and pattern recognition*, pages 11065–11074, 2019. 2
- [10] Mauricio Delbracio, Hossein Talebei, and Pevman Milanfar. Projected distribution loss for image enhancement. In *2021 IEEE International Conference on Computational Photography (ICCP)*, pages 1–12. IEEE, 2021. 3
- [11] Xin Deng, Ren Yang, Mai Xu, and Pier Luigi Dragotti. Wavelet domain style transfer for an effective perception-distortion tradeoff in single image super-resolution. In *Proceedings of the IEEE/CVF international conference on computer vision*, pages 3076–3085, 2019. 1, 3, 7
- [12] Keyan Ding, Kede Ma, Shiqi Wang, and Eero P Simoncelli. Image quality assessment: Unifying structure and texture similarity. *IEEE transactions on pattern analysis and machine intelligence*, 44(5):2567–2581, 2020. 6
- [13] Chao Dong, Chen Change Loy, Kaiming He, and Xiaoou Tang. Image super-resolution using deep convolutional networks. *IEEE transactions on pattern analysis and machine intelligence*, 38(2):295–307, 2015. 2
- [14] Chao Dong, Chen Change Loy, and Xiaoou Tang. Accelerating the super-resolution convolutional neural network. In *Computer Vision—ECCV 2016: 14th European Conference, Amsterdam, The Netherlands, October 11–14, 2016, Proceedings, Part II 14*, pages 391–407. Springer, 2016. 6
- [15] Ian Goodfellow, Jean Pouget-Abadie, Mehdi Mirza, Bing Xu, David Warde-Farley, Sherjil Ozair, Aaron Courville, and Yoshua Bengio. Generative adversarial nets. *Advances in neural information processing systems*, 27, 2014. 2
- [16] Xiangyu He, Zitao Mo, Peisong Wang, Yang Liu, Mingyuan Yang, and Jian Cheng. Ode-inspired network design for single image super-resolution. In *Proceedings of the IEEE/CVF Conference on Computer Vision and Pattern Recognition*, pages 1732–1741, 2019. 2
- [17] Martin Heusel, Hubert Ramsauer, Thomas Unterthiner, Bernhard Nessler, and Sepp Hochreiter. Gans trained by a two time-scale update rule converge to a local nash equilibrium. *Advances in neural information processing systems*, 30, 2017. 3
- [18] Chih-Chung Hsu, Chia-Ming Lee, and Yi-Shiuan Chou. Drct: Saving image super-resolution away from information bottleneck. *arXiv preprint arXiv:2404.00722*, 2024. 3, 4, 11, 12
- [19] Jia-Bin Huang, Abhishek Singh, and Narendra Ahuja. Single image super-resolution from transformed self-exemplars. In *Proceedings of the IEEE conference on computer vision and pattern recognition*, pages 5197–5206, 2015. 6
- [20] Sangeek Hyun and Jae-Pil Heo. Varsr: Variational super-resolution network for very low resolution images. In *Computer Vision—ECCV 2020: 16th European Conference, Glasgow, UK, August 23–28, 2020, Proceedings, Part XXIII*, pages 431–447. Springer, 2020. 2
- [21] Gareth M James. Variance and bias for general loss functions. *Machine learning*, 51:115–135, 2003. 3
- [22] Justin Johnson, Alexandre Alahi, and Li Fei-Fei. Perceptual losses for real-time style transfer and super-resolution. In *European conference on computer vision*, pages 694–711. Springer, 2016. 1, 2, 4
- [23] Tero Karras, Samuli Laine, and Timo Aila. A style-based generator architecture for generative adversarial networks. In *Proceedings of the IEEE/CVF conference on computer vision and pattern recognition*, pages 4401–4410, 2019. 3
- [24] Junjie Ke, Qifei Wang, Yilin Wang, Peyman Milanfar, and Feng Yang. Musiq: Multi-scale image quality transformer. In *Proceedings of the IEEE/CVF international conference on computer vision*, pages 5148–5157, 2021. 2
- [25] Jiwon Kim, Jung Kwon Lee, and Kyoung Mu Lee. Accurate image super-resolution using very deep convolutional networks. In *Proceedings of the IEEE conference on computer vision and pattern recognition*, pages 1646–1654, 2016. 2
- [26] Diederik P Kingma and Jimmy Ba. Adam: A method for stochastic optimization. *arXiv preprint arXiv:1412.6980*, 2014. 1

- [27] Idan Kligvasser and Tomer Michaeli. Sparsity aware normalization for gans. In *Proceedings of the AAAI Conference on Artificial Intelligence*, pages 8181–8190, 2021. 3
- [28] Idan Kligvasser, Tamar Shaham, Yuval Bahat, and Tomer Michaeli. Deep self-dissimilarities as powerful visual fingerprints. *Advances in Neural Information Processing Systems*, 34, 2021. 3
- [29] Denis Kuznedelev, Valerii Startsev, Daniil Shlenskii, and Sergey Kastrulin. Does diffusion beat gan in image super resolution? *arXiv preprint arXiv:2405.17261*, 2024. 3
- [30] Christian Ledig, Lucas Theis, Ferenc Huszár, Jose Caballero, Andrew Cunningham, Alejandro Acosta, Andrew Aitken, Alykhan Tejani, Johannes Totz, Zehan Wang, et al. Photo-realistic single image super-resolution using a generative adversarial network. In *Proceedings of the IEEE conference on computer vision and pattern recognition*, pages 4681–4690, 2017. 1, 2, 3, 8
- [31] MinKyu Lee and Jae-Pil Heo. Noise-free optimization in early training steps for image super-resolution. In *Proceedings of the AAAI Conference on Artificial Intelligence*, pages 2920–2928, 2024. 1, 3
- [32] Soochan Lee, Junsoo Ha, and Gunhee Kim. Harmonizing maximum likelihood with gans for multimodal conditional generation. *arXiv preprint arXiv:1902.09225*, 2019. 3
- [33] Bingchen Li, Xin Li, Hanxin Zhu, Yeying Jin, Ruoyu Feng, Zhizheng Zhang, and Zhibo Chen. Sed: Semantic-aware discriminator for image super-resolution. In *Proceedings of the IEEE/CVF Conference on Computer Vision and Pattern Recognition*, pages 25784–25795, 2024. 3
- [34] Wenbo Li, Xin Lu, Shengju Qian, Jiangbo Lu, Xiangyu Zhang, and Jiaya Jia. On efficient transformer-based image pre-training for low-level vision. *arXiv preprint arXiv:2112.10175*, 2021. 2
- [35] Yawei Li, Kai Zhang, Jingyun Liang, Jiezhang Cao, Ce Liu, Rui Gong, Yulun Zhang, Hao Tang, Yun Liu, Denis Demandolx, et al. Lsdir: A large scale dataset for image restoration. In *Proceedings of the IEEE/CVF Conference on Computer Vision and Pattern Recognition*, pages 1775–1787, 2023. 6
- [36] Jingyun Liang, Jiezhang Cao, Guolei Sun, Kai Zhang, Luc Van Gool, and Radu Timofte. Swinir: Image restoration using swin transformer. In *Proceedings of the IEEE/CVF International Conference on Computer Vision*, pages 1833–1844, 2021. 2, 6, 1, 13, 14
- [37] Jie Liang, Hui Zeng, and Lei Zhang. Details or artifacts: A locally discriminative learning approach to realistic image super-resolution. In *Proceedings of the IEEE/CVF Conference on Computer Vision and Pattern Recognition*, pages 5657–5666, 2022. 3, 4, 5, 6, 7, 8, 1, 2
- [38] Bee Lim, Sanghyun Son, Heewon Kim, Seungjun Nah, and Kyoung Mu Lee. Enhanced deep residual networks for single image super-resolution. In *The IEEE Conference on Computer Vision and Pattern Recognition (CVPR) Workshops*, 2017. 6
- [39] Bee Lim, Sanghyun Son, Heewon Kim, Seungjun Nah, and Kyoung Mu Lee. Enhanced deep residual networks for single image super-resolution. In *Proceedings of the IEEE conference on computer vision and pattern recognition workshops*, pages 136–144, 2017. 2
- [40] Ze Liu, Yutong Lin, Yue Cao, Han Hu, Yixuan Wei, Zheng Zhang, Stephen Lin, and Baining Guo. Swin transformer: Hierarchical vision transformer using shifted windows. In *Proceedings of the IEEE/CVF international conference on computer vision*, pages 10012–10022, 2021. 2
- [41] Andreas Lugmayr, Martin Danelljan, Luc Van Gool, and Radu Timofte. Srrflow: Learning the super-resolution space with normalizing flow. In *Computer Vision–ECCV 2020: 16th European Conference, Glasgow, UK, August 23–28, 2020, Proceedings, Part V 16*, pages 715–732. Springer, 2020. 2
- [42] Cheng Ma, Yongming Rao, Jiwen Lu, and Jie Zhou. Structure-preserving image super-resolution. *IEEE transactions on pattern analysis and machine intelligence*, 44(11): 7898–7911, 2021. 2, 3, 6, 4
- [43] David Martin, Charless Fowlkes, Doron Tal, and Jitendra Malik. A database of human segmented natural images and its application to evaluating segmentation algorithms and measuring ecological statistics. In *Proceedings Eighth IEEE International Conference on Computer Vision. ICCV 2001*, pages 416–423. IEEE, 2001. 6
- [44] Yusuke Matsui, Kota Ito, Yuji Aramaki, Azuma Fujimoto, Toru Ogawa, Toshihiko Yamasaki, and Kiyoharu Aizawa. Sketch-based manga retrieval using manga109 dataset. *Multimedia Tools and Applications*, 76:21811–21838, 2017. 6, 3
- [45] Yiqun Mei, Yuchen Fan, and Yuqian Zhou. Image super-resolution with non-local sparse attention. In *Proceedings of the IEEE/CVF Conference on Computer Vision and Pattern Recognition*, pages 3517–3526, 2021. 2
- [46] Anish Mittal, Rajiv Soundararajan, and Alan C Bovik. Making a “completely blind” image quality analyzer. *IEEE Signal processing letters*, 20(3):209–212, 2012. 2
- [47] Ben Niu, Weilei Wen, Wenqi Ren, Xiangde Zhang, Lianping Yang, Shuzhen Wang, Kaihao Zhang, Xiaochun Cao, and Haifeng Shen. Single image super-resolution via a holistic attention network. In *Computer Vision–ECCV 2020: 16th European Conference, Glasgow, UK, August 23–28, 2020, Proceedings, Part XII 16*, pages 191–207. Springer, 2020. 2
- [48] JoonKyu Park, Sanghyun Son, and Kyoung Mu Lee. Content-aware local gan for photo-realistic super-resolution. In *Proceedings of the IEEE/CVF International Conference on Computer Vision*, pages 10585–10594, 2023. 3, 6, 4, 15
- [49] Seung Ho Park, Young Su Moon, and Nam Ik Cho. Perception-oriented single image super-resolution using optimal objective estimation. In *Proceedings of the IEEE/CVF Conference on Computer Vision and Pattern Recognition*, pages 1725–1735, 2023. 3
- [50] Chitwan Saharia, Jonathan Ho, William Chan, Tim Salimans, David J Fleet, and Mohammad Norouzi. Image super-resolution via iterative refinement. *IEEE transactions on pattern analysis and machine intelligence*, 45(4):4713–4726, 2022. 3
- [51] Karen Simonyan and Andrew Zisserman. Very deep convolutional networks for large-scale image recognition. *arXiv preprint arXiv:1409.1556*, 2014. 7
- [52] Jianyi Wang, Kelvin CK Chan, and Chen Change Loy. Exploring clip for assessing the look and feel of images. In *Pro-*

- ceedings of the AAAI Conference on Artificial Intelligence, pages 2555–2563, 2023. 2
- [53] Jianyi Wang, Zongsheng Yue, Shangchen Zhou, Kelvin CK Chan, and Chen Change Loy. Exploiting diffusion prior for real-world image super-resolution. *International Journal of Computer Vision*, pages 1–21, 2024. 3
- [54] Xintao Wang, Ke Yu, Shixiang Wu, Jinjin Gu, Yihao Liu, Chao Dong, Yu Qiao, and Chen Change Loy. ESRGAN: Enhanced super-resolution generative adversarial networks. In *Proceedings of the European conference on computer vision (ECCV) workshops*, pages 0–0, 2018. 1, 3, 4, 5, 6, 2, 9, 10, 15
- [55] Xintao Wang, Liangbin Xie, Chao Dong, and Ying Shan. Real-esrgan: Training real-world blind super-resolution with pure synthetic data. In *Proceedings of the IEEE/CVF International Conference on Computer Vision*, pages 1905–1914, 2021. 1, 2
- [56] Xintao Wang, Liangbin Xie, Ke Yu, Kelvin C.K. Chan, Chen Change Loy, and Chao Dong. BasicSR: Open source image and video restoration toolbox. <https://github.com/XPixelGroup/BasicSR>, 2022. 1
- [57] Zhou Wang, Alan C Bovik, Hamid R Sheikh, and Eero P Simoncelli. Image quality assessment: from error visibility to structural similarity. *IEEE transactions on image processing*, 13(4):600–612, 2004. 6
- [58] Pengxu Wei, Ziwei Xie, Hannan Lu, Zongyuan Zhan, Qixiang Ye, Wangmeng Zuo, and Liang Lin. Component divide-and-conquer for real-world image super-resolution. In *Computer Vision—ECCV 2020: 16th European Conference, Glasgow, UK, August 23–28, 2020, Proceedings, Part VIII 16*, pages 101–117. Springer, 2020. 7, 2
- [59] Liangbin Xie, Xintao Wang, Xiangyu Chen, Gen Li, Ying Shan, Jiantao Zhou, and Chao Dong. Desra: Detect and delete the artifacts of gan-based real-world super-resolution models. 2023. 3, 4
- [60] Sidi Yang, Tianhe Wu, Shuwei Shi, Shanshan Lao, Yuan Gong, Mingdeng Cao, Jiahao Wang, and Yujiu Yang. Maniqa: Multi-dimension attention network for no-reference image quality assessment. In *Proceedings of the IEEE/CVF Conference on Computer Vision and Pattern Recognition*, pages 1191–1200, 2022. 2
- [61] Fanghua Yu, Jinjin Gu, Zheyuan Li, Jinfan Hu, Xiangtao Kong, Xintao Wang, Jingwen He, Yu Qiao, and Chao Dong. Scaling up to excellence: Practicing model scaling for photo-realistic image restoration in the wild. In *Proceedings of the IEEE/CVF Conference on Computer Vision and Pattern Recognition*, pages 25669–25680, 2024. 3
- [62] Roman Zeyde, Michael Elad, and Matan Protter. On single image scale-up using sparse-representations. In *International conference on curves and surfaces*, pages 711–730. Springer, 2010. 6
- [63] Dafeng Zhang, Feiyu Huang, Shizhuo Liu, Xiaobing Wang, and Zhezhu Jin. Swinir: Revisiting the swinir with fast fourier convolution and improved training for image super-resolution. *arXiv preprint arXiv:2208.11247*, 2022. 2
- [64] Kai Zhang, Luc Van Gool, and Radu Timofte. Deep unfolding network for image super-resolution. In *Proceedings of the IEEE/CVF Conference on Computer Vision and Pattern Recognition (CVPR)*, 2020. 2
- [65] Kai Zhang, Jingyun Liang, Luc Van Gool, and Radu Timofte. Designing a practical degradation model for deep blind image super-resolution. In *Proceedings of the IEEE/CVF International Conference on Computer Vision*, pages 4791–4800, 2021. 1, 2
- [66] Richard Zhang, Phillip Isola, Alexei A Efros, Eli Shechtman, and Oliver Wang. The unreasonable effectiveness of deep features as a perceptual metric. In *Proceedings of the IEEE conference on computer vision and pattern recognition*, pages 586–595, 2018. 6, 1
- [67] Wenlong Zhang, Yihao Liu, Chao Dong, and Yu Qiao. Rankrgan: Generative adversarial networks with ranker for image super-resolution. In *Proceedings of the IEEE/CVF International Conference on Computer Vision*, pages 3096–3105, 2019. 2
- [68] Yulun Zhang, Kunkeng Li, Kai Li, Lichen Wang, Bineng Zhong, and Yun Fu. Image super-resolution using very deep residual channel attention networks. In *Proceedings of the European conference on computer vision (ECCV)*, pages 286–301, 2018. 2
- [69] Yuehan Zhang, Bo Ji, Jia Hao, and Angela Yao. Perception-distortion balanced admm optimization for single-image super-resolution. In *European Conference on Computer Vision*, pages 108–125. Springer, 2022. 1, 3, 7
- [70] Shangchen Zhou, Jiawei Zhang, Wangmeng Zuo, and Chen Change Loy. Cross-scale internal graph neural network for image super-resolution. *Advances in neural information processing systems*, 33:3499–3509, 2020. 2

Auto-Encoded Supervision for Perceptual Image Super-Resolution

Supplementary Material

A. Implementation and experimental details

Network architecture and weight initialization. Following previous works, we initialize our SR networks with the official weight of the fidelity-oriented model of either ESRGAN [54] or SwinIR [36]. Similarly, the decoder of the AE follows the architecture of RRDB and is initialized with the fidelity-oriented weights. The overall architecture of the encoder is implemented in a straightforward manner. We simply design it as a series of two convolutional layers (fromRGB layer), followed by a pixel-unshuffle operation and two RRDB blocks [54], concluding with additional two convolutional layers (toRGB layer). The RRDB block is identical to that of the SR networks. The pixel-unshuffle acts as a $\times s$ downscaling operation, effectively reducing the image dimension to match that of the LR image. Since the channel size is increased due to the pixel-shuffle operation, the second layer of the fromRGB layer reduces the channel size $\times s^2$ smaller than that of the RRDB block. The kernel size is 3×3 for all convolutional layers.

Training and evaluation details. The optimizer is chosen as the Adam [26] optimizer with a learning rate of 0.0001, for both the Auto-Encoder and the SR network. Following conventions, we choose $p = 1$ for \mathcal{L}_p and the coefficient of loss factors are $\lambda_{\text{AESOP}} = 1$, $\lambda_2 = 1$, $\lambda_3 = 1$, $\lambda_4 = 0.005$. The Auto-Encoder is pretrained up to 100K iterations, and the SR networks are trained up to 300K iterations. Unless specified, the HR training patch size is 128. PSNR and SSIM scores are evaluated on the Y channel (luminance channel) in the YCbCr space and pixels up to the scale factors in the border were ignored. We use the default `alex` option for LPIPS [66]. Training and evaluation are performed on top of BasicSR [56]. Networks are trained and evaluated with either 4 NVIDIA A6000s or 4 NVIDIA RTX 3090s.

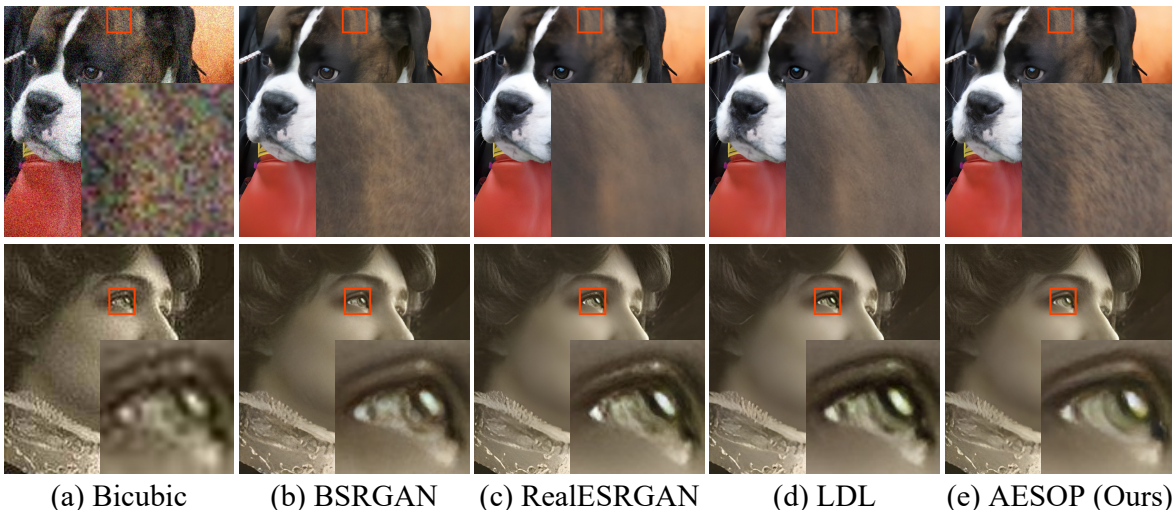


Figure 7. Visual comparison between AESOP (ours) against baseline methods for the real-world $\times 4$ SR task. AESOP leads to improved realism (top) with a lower level of visual artifacts (bottom). **Zoom in for best view.**

B. Evaluation on real-world SR datasets

AESOP on real-world SR. In the real-world SR task, the overall task becomes more complex and the range of plausible solutions is larger than that of the conventional bicubic SR task. Accordingly, the conflict between \mathcal{L}_{pix} and perceptual quality-oriented objectives gets severe, and the blurring tendency of conventional \mathcal{L}_{pix} loss may become more significant. We further validate the effectiveness of the proposed method in the real-world $\times 4$ SR task. For comparison, we use representative baseline real-world SR methods utilizing \mathcal{L}_{pix} , including RealESRGAN [55], BSRGAN [65], and LDL [37].

Dataset	Method	NIQE↓	MANIQA	MUSIQ	CLIP-IQA
RealSRv3 [3]	ESRGAN [54]	7.7326	0.2043	29.0494	0.2362
	BSRGAN [65]	4.6519	0.3698	63.5908	0.5439
	Real-ESRGAN [55]	4.6790	0.3662	59.6855	0.4901
	LDL [37]	4.8869	0.3706	60.1015	0.4883
	AESOP (Ours)	4.2337	0.4136	63.6489	0.5687
DRealSR [58]	ESRGAN [54]	8.3949	0.2115	20.2861	0.2468
	BSRGAN [65]	4.6809	0.3381	35.4973	0.5614
	Real-ESRGAN [55]	4.7152	0.3404	35.2747	0.5098
	LDL [37]	5.0974	0.3393	35.9026	0.5137
	AESOP (Ours)	4.1922	0.3917	36.5533	0.6025

Table 6. Quantitative results of AESOP and baseline methods in real-world settings. All methods except ESRGAN are trained for the real-world SR task. The best results of each group are highlighted in **bold**. ↓ means lower is better. If not specified, higher is better. Due to memory constraints, images were cropped before evaluating CLIP-IQA scores for the DRealSR dataset.

Backbone		RRDB						SwinIR			
Metrics	Benchmark	ESRGAN	SPSR	LDL*	LDL	AESOP	AESOP	+GAN	LDL*	LDL	AESOP
Recon. Objective		\mathcal{L}_{pix}	\mathcal{L}_{pix}	\mathcal{L}_{pix}	\mathcal{L}_{pix}	$\mathcal{L}_{\text{AESOP}}$	$\mathcal{L}_{\text{AESOP}}$	\mathcal{L}_{pix}	\mathcal{L}_{pix}	\mathcal{L}_{pix}	$\mathcal{L}_{\text{AESOP}}$
Patch size (Training)		128	128	128	128	128	256	256	256	256	256
pFID ↓	Set14	65.220	70.990	-	57.132	56.727	54.792	-	-	55.367	53.175
	Manga109	29.326	28.314	-	23.895	23.384	22.833	-	-	21.766	21.290
	General100	50.062	50.053	-	43.406	42.117	41.041	-	-	42.028	40.199
	Urban100	32.094	31.105	-	28.380	27.875	27.017	-	-	26.972	25.613
	BSD100	69.943	68.370	-	64.058	57.864	56.844	-	-	59.653	57.118
	LSDIR	14.579	14.110	-	12.537	12.220	11.718	-	-	12.056	11.387
FID ↓	Set14	54.939	53.919	43.454	43.479	46.828	38.907	48.910	46.057	46.110	45.411
	Manga109	11.559	10.663	10.161	10.162	9.230	9.446	9.703	8.680	8.677	9.256
	General100	29.850	30.172	27.211	27.220	27.425	25.201	27.557	25.304	25.301	24.592
	Urban100	20.354	18.676	16.351	16.355	16.865	16.723	17.555	16.282	16.287	15.547
	BSD100	50.752	48.349	-	44.053	41.130	40.751	-	-	41.954	41.721
	LSDIR	17.552	16.056	-	15.229	14.748	14.802	-	-	14.510	14.397

Table 7. Quantitative results of the proposed method (AESOP) against baseline methods. We report Frechet Inception Distance (FID) and patch-FID (pFID) scores. LDL* indicates that scores are from the official paper. All other scores are evaluated in our settings, with officially provided pretrained weights. The best results of each group are highlighted in **bold**, based on scores evaluated in our settings.

Qualitative results. In Fig.7, we provide a visual comparison of AESOP against baseline methods for the $\times 4$ real-world SISR task on RealSRSet [65]. We only replace the \mathcal{L}_{pix} term of [37] while keeping all other training settings identical. Since we do not have ground-truth HR images, we only provide bicubic upsampled images and SR results from each method. Due to the inherent high complexity of the real-world task, baseline networks fail in generating fine-grained textures (first row of Fig.7) and generate visually unpleasing artifacts (second row of Fig.7). In contrast, AESOP successfully recovers fine textures with fewer artifacts.

Quantitative results. We report quantitative results on RealSRv3 [3] and DRealSR [58]. To assess perceptual quality, we utilize NIQE [46], MANIQA [60], MUSIQ [24], and CLIP-IQA [52] scores. Due to memory constraints, images were divided into four quadrants when evaluating the CLIP-IQA scores for the DRealSR dataset. AESOP demonstrates superior performance against baselines in all evaluation metrics, which verifies the effectiveness of our method for practical applications.

C. Additional results for the bicubic SR task

FID scores. In Tab.7, we report Frechet Inception Distance (FID) [17] scores to further evaluate the proposed AESOP against baseline methods for the bicubic $\times 4$ SR task. FID, widely used for generative tasks [23], has recently been adopted for super-resolution tasks [37, 48]. However, its standard approach of resizing images to 299×299 may not be suitable to assess SR methods. Resizing can alter important details that SR aims to improve, directly conflicting with the objectives of SR focusing on enhancing image quality at higher resolutions.

Patch FID scores. Accordingly, we additionally report the patch-FID (pFID) [4] scores, which does not require image resizing. For patch-FID evaluation, 299×299 non-overlapping patches are extracted from the images. If an image is smaller than 299 pixels in any dimension, we use zero-padding to meet the required size.

Fidelity bias estimation. As discussed in the main article, we do not multiply a small scaling factor to $\mathcal{L}_{\text{AESOP}}$ which leads to significantly stronger guidance on fidelity biases (Fig.9). Accordingly, we have measured how well AESOP and the baseline methods estimate the fidelity biases by reporting AE-PSNR which captures the distance between the fidelity bias of the SR image and the fidelity bias of the HR image. Additionally, we have shown LR-PSNR scores to provide a metric that is not biased by the Auto-Encoder. In Tab.9, we additionally provide AE-PSNR and LR-PSNR scores on top of the RRDB [54] backbone. Similar to results in Tab.4, AESOP shows improvements in both AE-PSNR and LR-PSNR scores, highlighting the superiority of AESOP in effectively reducing the SE term.

AESOP on recent backbone network architecture. We report additional quantitative results on the benchmark datasets in Tab.8. First, we employ DRCT [18], a recent state-of-the-art method that enhances the network architecture within the fidelity-oriented SR framework. We reproduce LDL on top of DRCT, and compare it with $\mathcal{L}_{\text{AESOP}}$. AESOP is shown to be effective in these recent network architectures as well, outperforming the baseline in both fidelity and perceptual quality.

Regarding recent perceptual-oriented losses. We report quantitative results of another recent state-of-the-art method, CALGAN [48]. This work is a different branches of research in the field of perceptual SR, focusing on improvements in perceptual quality-oriented losses. Interestingly, AESOP outperforms CALGAN in most cases, even without the Mixture of Experts (MoE)-based discriminator proposed in CALGAN [48]. This signifies the effectiveness of AESOP. However, note that improvements in network architectures and perceptual-oriented losses are beyond the scope of this work. The focus of this study is on the fidelity loss term \mathcal{L}_{pix} within the perceptual SR framework. We leave the integration of $\mathcal{L}_{\text{AESOP}}$ (fundamentally a *fidelity* loss), with the enhanced perceptual-oriented losses of CALGAN to future work due to limited computational budget.

Additional perception-distortion trade-off curves. We provide extensive visualizations of the perception-distortion trade-off curves in Fig.12-18. For CALGAN [48], we present only a single data point rather than the full perception-distortion trade-off curve, as its official weights are not publicly available. Extensive results show that AESOP leads to substantial performance improvements against baselines in terms of the perception-distortion trade-off. Aligning to Tab.8, AESOP also often outperforms CALGAN even without MoE-discriminator proposed in CALGAN. Additionally, we observe that AESOP often results in larger improvements for Swin Transformer-based methods (e.g., SwinIR, DRCT) compared to CNN-based methods (e.g., RRDB). This is likely because these models have greater capacity and benefit more from the enhanced reconstruction guidance provided by AESOP. However, there are instances where AESOP does not always lead to improved performance. Specifically, AESOP often fails to enhance performance on the Manga109 [44] dataset, which is consistent with the unexpected trade-off behaviors observed across most methods in this dataset. This limitation arises because Manga109 consists predominantly of comic images, which typically lack the fine-grained textures found in photorealistic datasets. The absence of such textures poses a challenge for perceptual SR methods, including AESOP, which are specifically designed to enhance and preserve realistic textures. Consequently, without the presence of these detailed textures, AESOP’s advantages in minimizing fidelity bias and preserving perceptual variance are less pronounced, leading to suboptimal performance in this particular dataset.

Backbone		RRDB		SwinIR		DRCT	
Metrics	Benchmark	CALGAN	AESOP	CALGAN	AESOP	LDL	AESOP
Recon. Objective		\mathcal{L}_{pix}	$\mathcal{L}_{\text{AESOP}}$	\mathcal{L}_{pix}	$\mathcal{L}_{\text{AESOP}}$	\mathcal{L}_{pix}	$\mathcal{L}_{\text{AESOP}}$
LPIPS ↓	Set14	-	0.1053	-	0.1027	0.1086	0.1022
	Manga109	-	0.0494	-	0.0461	0.0459	0.0447
	General100	0.077	0.0734	0.074	0.0710	0.0727	0.0722
	Urban100	0.108	0.1033	0.098	0.0945	0.1006	0.0972
	DIV2K-val	0.091	0.0936	0.087	0.0893	0.0934	0.0949
	BSD100	0.151	0.1443	0.147	0.1385	0.1462	0.1451
	LSDIR	-	0.1123	-	0.1071	0.1131	0.1129
DISTS ↓	Set14	-	0.0825	-	0.0819	0.0889	0.0830
	Manga109	-	0.0356	-	0.0328	0.0316	0.0338
	General100	0.083	0.0773	0.081	0.0762	0.0782	0.0775
	Urban100	0.082	0.0768	0.083	0.0742	0.0803	0.0771
	DIV2K-val	0.049	0.0484	0.048	0.0459	0.0487	0.0485
	BSD100	0.118	0.1089	0.128	0.1072	0.1136	0.1072
	LSDIR	-	0.0612	-	0.0591	0.0635	0.0621
PSNR ↑	Set14	-	27.246	-	27.421	27.314	27.796
	Manga109	-	29.747	-	30.061	29.979	30.398
	General100	30.182	30.251	-	30.401	30.143	30.646
	Urban100	25.290	25.541	-	26.148	26.038	26.360
	DIV2K-val	28.863	28.910	-	29.137	29.030	29.456
	BSD100	25.925	25.904	-	25.930	25.942	26.324
	LSDIR	-	24.845	-	25.038	24.943	25.354
SSIM ↑	Set14	-	0.7371	-	0.7438	0.7403	0.7546
	Manga109	-	0.8802	-	0.8880	0.8888	0.8936
	General100	0.825	0.8269	-	0.8327	0.8288	0.8382
	Urban100	0.763	0.7697	-	0.7884	0.7855	0.7926
	DIV2K-val	0.790	0.7951	-	0.8023	0.7994	0.8085
	BSD100	0.676	0.6783	-	0.6813	0.6812	0.6921
	LSDIR	-	0.7202	-	0.7289	0.7253	0.7353

Table 8. Additional quantitative evaluation on benchmark datasets. We also provide quantitative results of CALGAN [48] and DRCT [18]. CALGAN is a recent work improving perceptual-oriented losses, while DRCT made improvements in the SR network architecture. AESOP mostly outperforms CALGAN [48] even without the MoE-discriminator. However, note that enhancements to network architectures and perceptual-oriented losses are beyond the scope of this work. The focus of this work is on the fidelity loss term \mathcal{L}_{pix} under the perceptual SR framework. The best results of each group are highlighted in **bold**. Additionally, refer to the PD trade-off curve in Fig.12-18.

Metric	Method	Set14	Mg109	Gen100	Urb100	DIV2K	B100	LSDIR
AE-PSNR	ESRGAN [54]	30.280	31.165	32.663	27.198	31.668	28.991	27.636
	SPSR [42]	30.602	31.351	32.670	27.508	31.737	29.029	27.881
	LDL [37]	31.180	32.608	33.823	28.488	32.597	29.595	28.625
	AESOP (Ours)	31.341	32.843	33.956	28.529	32.740	29.737	28.812
LR-PSNR	ESRGAN [54]	43.892	43.908	45.259	42.879	45.689	43.823	42.718
	SPSR [42]	43.835	44.359	44.656	42.666	44.717	42.719	42.364
	LDL [37]	46.497	47.603	48.184	45.975	47.793	45.307	45.295
	AESOP (Ours)	46.625	48.188	48.653	46.280	48.272	45.837	45.571

Table 9. AE-PSNR and LR-PSNR scores on the RRDB-backbone.

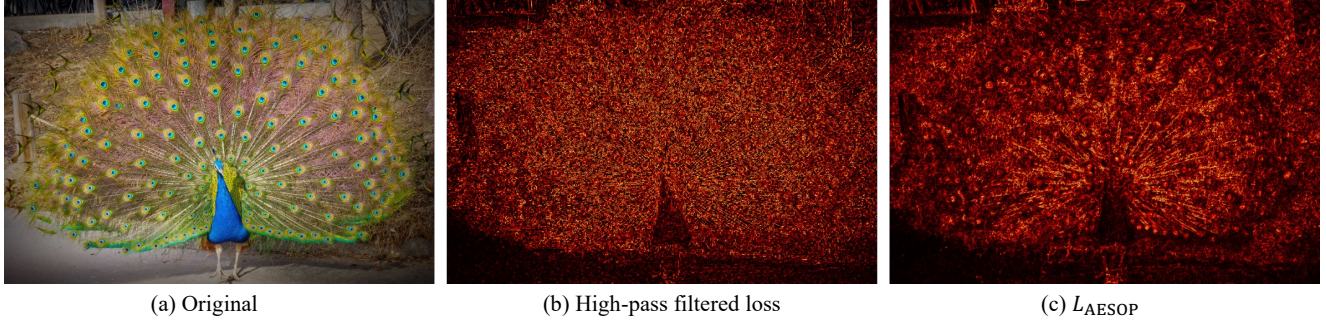


Figure 8. Loss map comparison between high-pass filtered (HPF) loss and $\mathcal{L}_{\text{AESOP}}$. Refer to Appendix.E for further discussion.

D. Additional visualization

Qualitative examples on benchmark datasets. To further illustrate the effectiveness of our method, we present an additional qualitative comparison between AESOP against the baseline method LDL [37] on the bicubic $\times 4$ SR task. We provide results of tested methods, AESOP and LDL, on top of the SwinIR backbone (Fig.20 and Fig.21) and the RRDB backbone (Fig.22 and Fig.23). As can be seen, the proposed AESOP significantly improves the perceptual quality while effectively suppressing visual artifacts observed in the baseline method.

Spectral magnitudes. Fig.19 provides visual examples of the spectral magnitudes, aligning with Fig.6. The spectral magnitudes reflect the effectiveness of the pretrained Auto-Encoder in discriminating non-regressable factors that lead to blurring and the regressable high-frequency components that enhance fidelity without causing blurring. Meanwhile, low-pass filters fail to achieve this since the regressable and non-regressable components cannot be disentangled using simple frequency filters. They are intertwined within the same frequency band.

E. Further discussion on AESOP

Regarding the loss maps and spectral magnitudes. Here we provide further discussions regarding the loss maps and the spectral analysis in the main article. In Sec.5.2, we have discussed the differences between AESOP and *low*-pass filtering-based methods. However, the loss maps reveal object edges, which are the regressable high-frequency components, aligning to *high*-pass filters. Accordingly, we provide further discussion and compare AESOP against high-pass filter based losses or similarly against edge filters from two perspectives: 1) regions with low loss values under $\mathcal{L}_{\text{AESOP}}$ and 2) regions with high loss values under HPF losses. (Fig.8)

First, we emphasize that regions with low loss values under $\mathcal{L}_{\text{AESOP}}$ do not imply that $\mathcal{L}_{\text{AESOP}}$ neglects these areas. Instead, they simply indicate that the network has accurately estimated the fidelity bias in those regions. This is clearly different from frequency filters, which entirely ignore these regions. For instance, consider a scenario where the SR network produces low-frequency artifacts due to adversarial training instability. In such cases, $\mathcal{L}_{\text{AESOP}}$ effectively guides the network toward proper estimation, whereas HPF loss ignores these artifacts, resulting in suboptimal performance. This also suggests that the components that require reconstruction guidance and those that do not require reconstruction guidance are inherently intertwined within each pixel. Thus, they cannot be disentangled merely by selecting which pixels to penalize.

Meanwhile, for regions that receive high loss activations under high-pass filtering (HPF) loss, these typically correspond to areas with fine textures. This is exactly the problematic issue raised in \mathcal{L}_{pix} , where such activations contribute to blurring. Consequently, this represents an undesirable aspect of HPF-based methods.

Intuitions on $\mathcal{L}_{\text{AESOP}}$ based on loss scales. In Fig.9, we compare the loss scales of \mathcal{L}_{pix} and $\mathcal{L}_{\text{AESOP}}$, both before and after applying their loss coefficients. Before the loss coefficients are applied, \mathcal{L}_{pix} (green) exhibits greater loss values than $\mathcal{L}_{\text{AESOP}}$ (blue). This observation aligns with our theoretical analysis and construction of the Auto-Encoder, where $\mathcal{L}_{\text{AESOP}}$ only penalizes a subcomponent of \mathcal{L}_{pix} . Specifically, while \mathcal{L}_{pix} minimizes both perceptual variance (VE) and fidelity bias induced error (SE), our carefully designed $\mathcal{L}_{\text{AESOP}}$ only targets the SE term, leading to lower loss values. Consequently, the gap between the green loss trajectory and the blue one quantifies the VE loss component embedded within \mathcal{L}_{pix} . When the loss coefficients are applied, $\mathcal{L}_{\text{AESOP}}$ (blue) provides an order of magnitude stronger reconstruction guidance compared to scaled \mathcal{L}_{pix} (red). Regardless of this increased fidelity guidance, SR networks trained with $\mathcal{L}_{\text{AESOP}}$ do not have to suffer from blurring and can achieve improved perceptual quality over \mathcal{L}_{pix} .

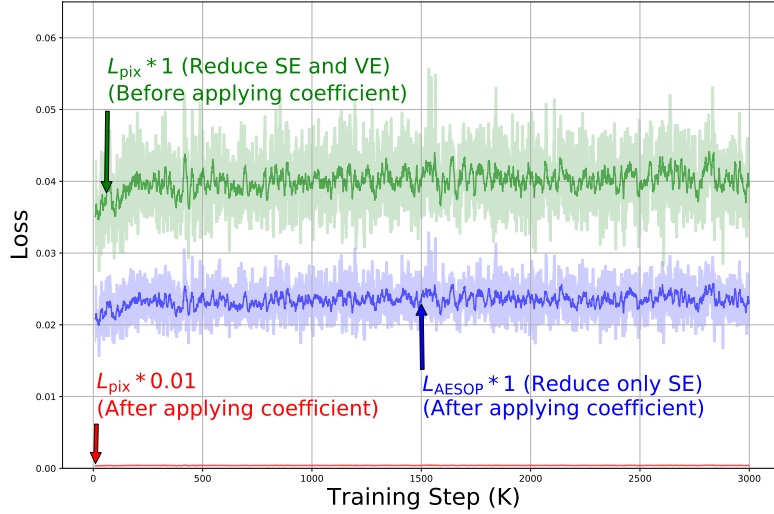


Figure 9. Loss scale comparison between \mathcal{L}_{pix} and $\mathcal{L}_{\text{AESOP}}$, before and after applying the loss coefficients of each. The loss trajectory of \mathcal{L}_{pix} before applying the coefficient (green) is visualized by scaling the original loss (red). The loss trajectory of $\mathcal{L}_{\text{AESOP}}$ is visualized as-is, since we do not scale it. Refer to Appendix.E for further discussion.

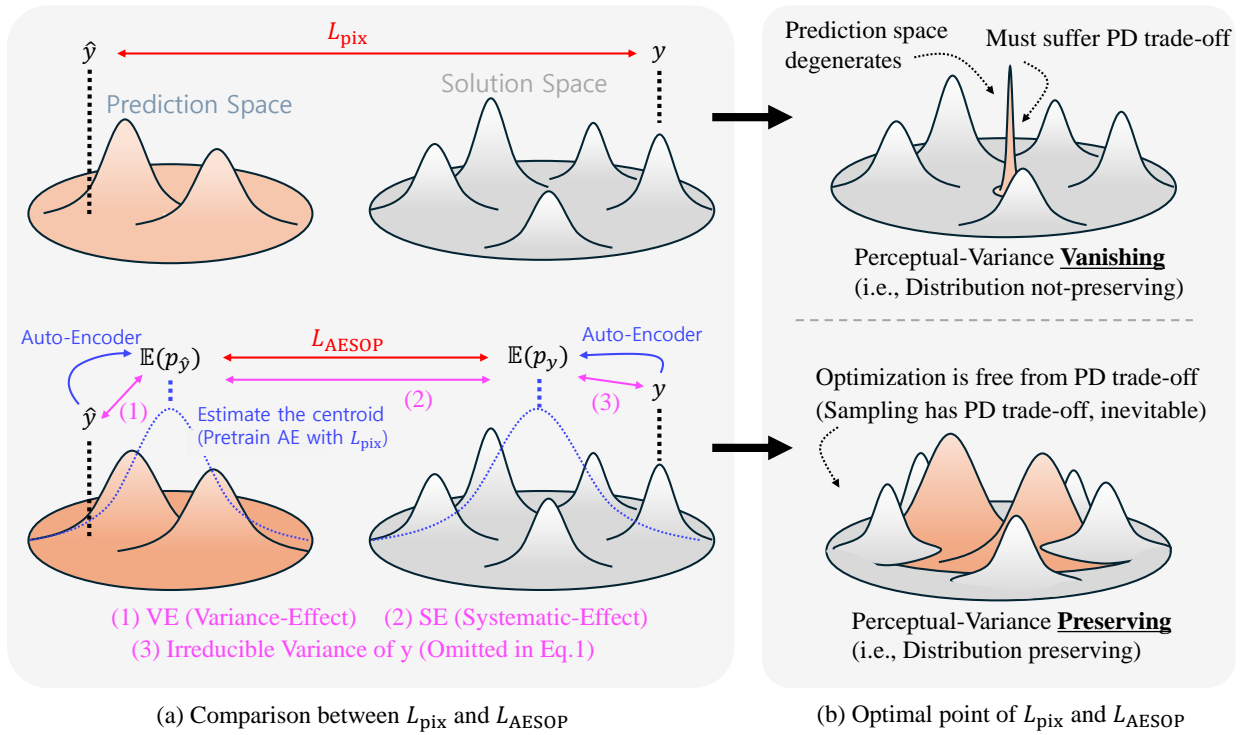


Figure 10. Graphical illustration of the optimization procedure and the optimal point for \mathcal{L}_{pix} and $\mathcal{L}_{\text{AESOP}}$.

Intuitions on \mathcal{L}_{pix} and $\mathcal{L}_{\text{AESOP}}$. Apart from Fig.1, we show additional graphical illustration in Fig.10 to provide further intuitions on the overall optimization procedure and the optimal point of each \mathcal{L}_{pix} and $\mathcal{L}_{\text{AESOP}}$. As can be seen, $\mathcal{L}_{\text{AESOP}}$ consecutively estimates the centroid (fidelity bias) of the prediction and solution space, and minimizes the distance between them (i.e., minimizes the SE factor). Accordingly, $\mathcal{L}_{\text{AESOP}}$ reaches the optimal point when the two distributions are aligned. However, \mathcal{L}_{pix} converges to the minimum expected error point, which is the blurry average solution. Thus, the prediction space degenerates.

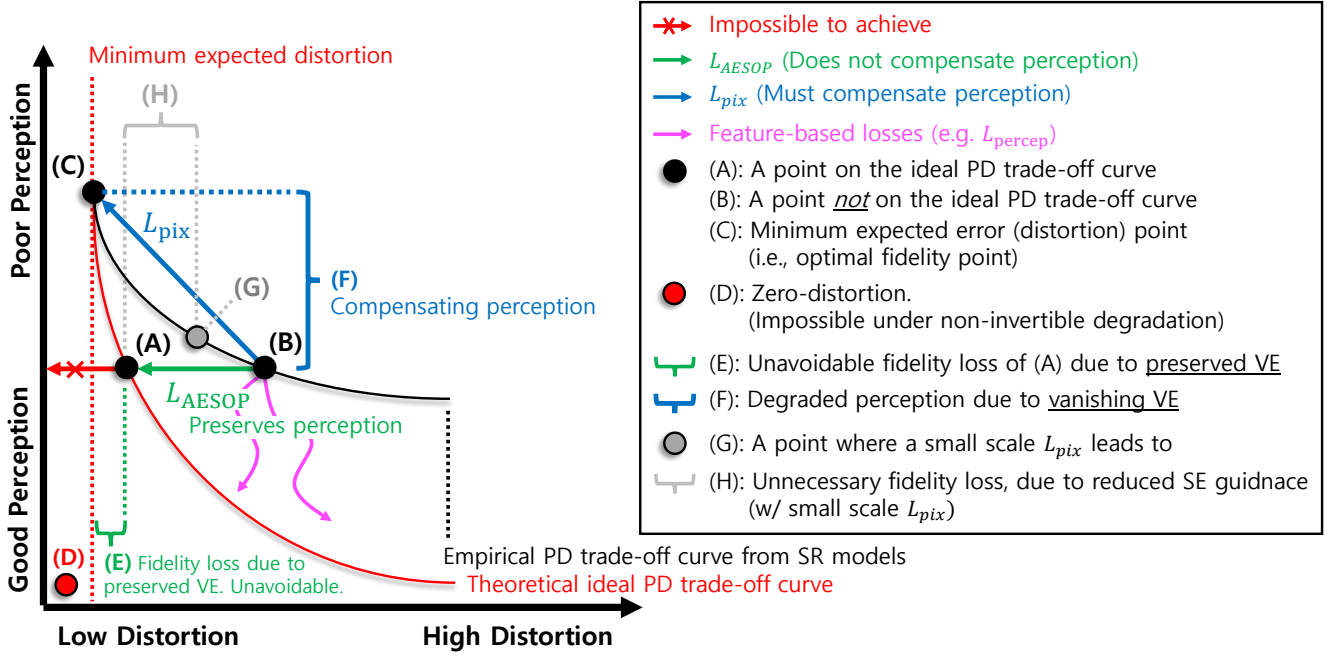


Figure 11. Graphical illustration of \mathcal{L}_{pix} and \mathcal{L}_{AESOP} in terms of the perception-distortion trade-off.

F. Understanding AESOP in terms of PD trade-off

Comparison between \mathcal{L}_{pix} and \mathcal{L}_{AESOP} . Fig. 11 represents the guidance \mathcal{L}_{pix} and \mathcal{L}_{AESOP} provides in terms the perception-distortion (PD) trade-off. We start our discussion with point (B), which represents an image that is not optimal in both fidelity and perception. Given this image, \mathcal{L}_{pix} with a large coefficient guides the image towards point (C). This is the blurry image with the lowest expected distortion, or simply the fidelity bias of the image. Meanwhile, with a smaller coefficient, it achieves improved perception as point (G). However, it leads to unnecessary fidelity loss (H) since SE reduction is significantly weakened while the adversarial loss continuously hinders SE convergence. Meanwhile, \mathcal{L}_{AESOP} removes the VE minimization term of \mathcal{L}_{pix} . Thus, it improves fidelity without suffering from blurring, thereby guides point (B) towards point (A). However, we clarify that \mathcal{L}_{AESOP} cannot further improve the fidelity beyond the ideal PD trade-off curve. This is impossible as (E), under non-invertible degradation [2] including image super-resolution. This statement even holds for the case with an optimal perceptual SR network that can sample images from the true posterior. Note that \mathcal{L}_{AESOP} reaches zero for point (A).

Comparison between \mathcal{L}_{percep} and \mathcal{L}_{AESOP} . The proposed loss \mathcal{L}_{AESOP} and \mathcal{L}_{percep} share the characteristic of utilizing a pre-trained neural network. However, the purpose of these two losses is fundamentally different. \mathcal{L}_{percep} falls within the category of perceptual-oriented losses, aiming for improved perception. Thus, it measures the distance between the SR image and the HR image in a space where additional semantics and textural information are expected to reside. This space is obtained by designing a feature extractor (VGG [51]) that has a *high-dimensional* feature space, that learns to generate *additional* semantics not present in the raw pixel space.

In contrast, \mathcal{L}_{AESOP} is fundamentally a reconstruction loss (fidelity loss), but tailored for the perceptual SR task so that it improves fidelity, for a given level of perception. It utilizes an Auto-Encoder which has a low-dimensional bottleneck. The dimension of the bottleneck is identical to the LR image, thus, the Auto-Encoder compresses and removes specific information. Here, the removed information is the perceptual variance, due to the pretraining objective and the architectural choice of the Auto-Encoder. Accordingly, the Auto-Encoded image contains *less* information than the raw image, contrary to the high-dimensional feature extractor in \mathcal{L}_{percep} . Note that the term *Auto-Encoded space* of \mathcal{L}_{AESOP} indicates the space after the decoder, not the bottleneck. Additionally, we clarify that the improvement in perceptual scores by raising \mathcal{L}_{AESOP} is since it does not hinder the perceptual-oriented guidance provided by perceptual-oriented losses under the SRGAN-framework. \mathcal{L}_{AESOP} as a standalone loss will not guide towards realism. We keep improvements in perceptual-oriented losses out of the scope of this work.

Is $\mathcal{L}_{\text{AESOP}}$ a distortion measure? Blau et. al. [2] have shown that we must compensate perception when aiming to reduce *any* distortion measure; the perception-distortion trade-off. This might seem contradictory with $\mathcal{L}_{\text{AESOP}}$ at first glance, since $\mathcal{L}_{\text{AESOP}}$ is designed to improve fidelity without degrading perception. However, fortunately, $\mathcal{L}_{\text{AESOP}}$ does not fall within the definition of distortion metric defined in Blau et. al. [2]. A distortion measure Δ that induces PD trade-off requires: $\Delta(y_1, y_2) > 0$ for $y_1 \neq y_2$ by definition. However, for AESOP, it is straightforward (and also intended) that multiple different images can share an identical fidelity bias. Formally, there exists y_1, y_2 s.t. $\mathcal{L}_{\text{AESOP}}(y_1, y_2) = 0$ and $y_1 \neq y_2$. As this does not satisfy the constraints of a distortion measure, $\mathcal{L}_{\text{AESOP}}$ is not guaranteed to raise PD trade-off. However, we clarify that this does not imply that SR networks trained with $\mathcal{L}_{\text{AESOP}}$ can generate images that are free from the PD trade-off. This is impossible even with an oracle perceptual SR network, as discussed in prior sections.

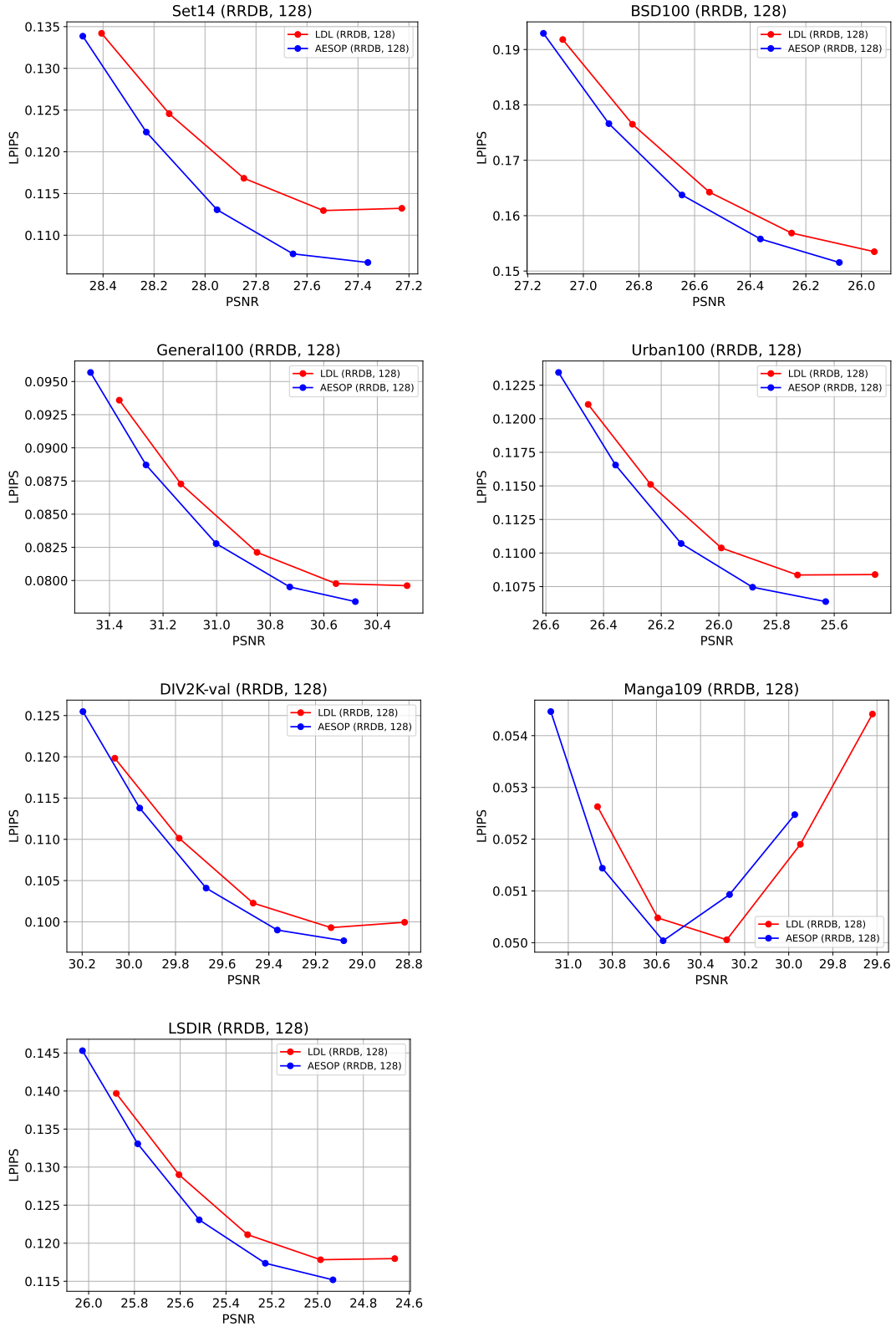


Figure 12. The perception-distortion trade-off curve between AESOP and baseline methods on top of the RRDB [54] backbone. The training HR patch size is 128. AESOP often fails to improve the performance on the Manga109 dataset.

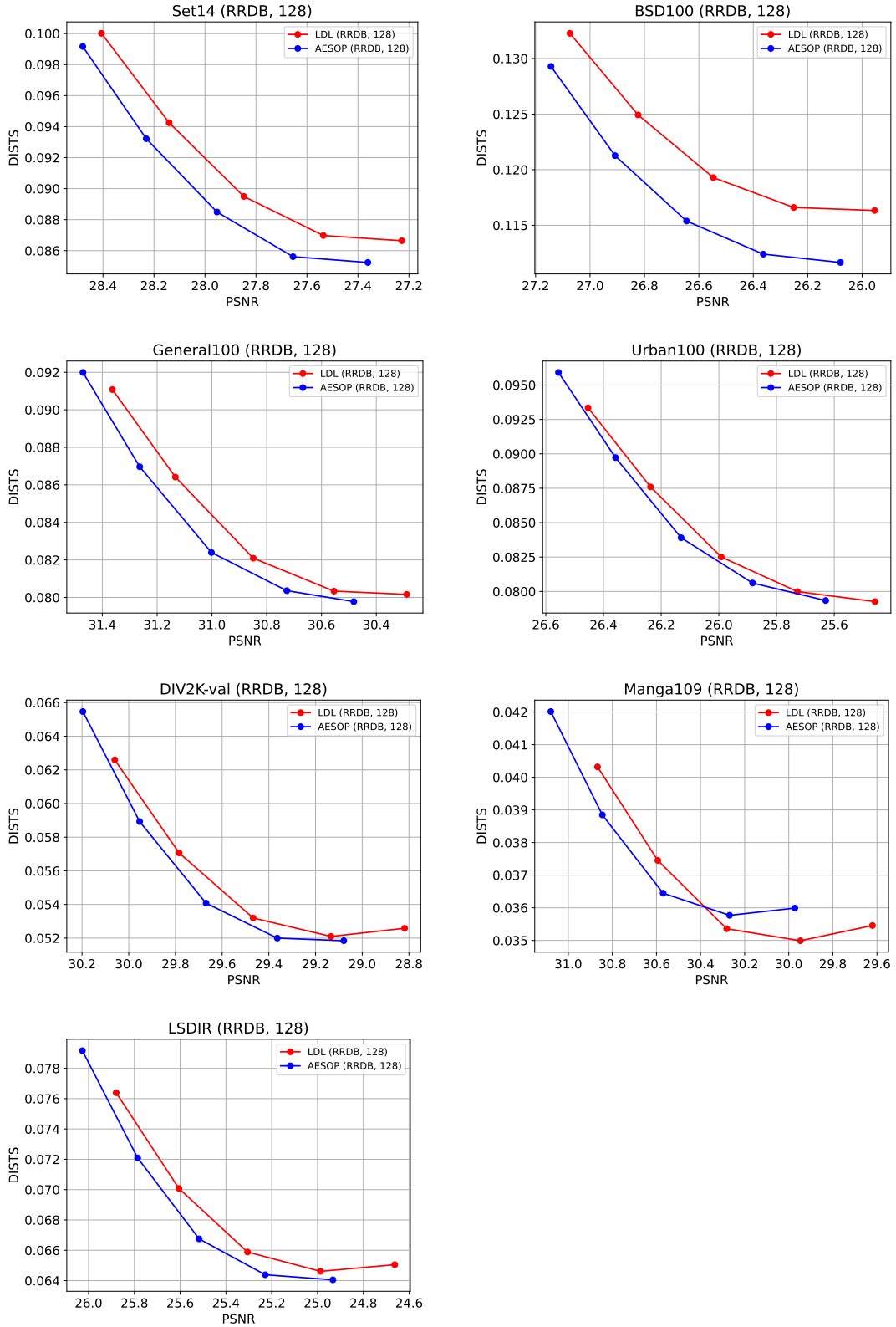


Figure 13. The perception-distortion trade-off curve between AESOP and baseline methods on top of the RRDB [54] backbone. The training HR patch size is 128. AESOP often fails to improve the performance on the Manga109 dataset.

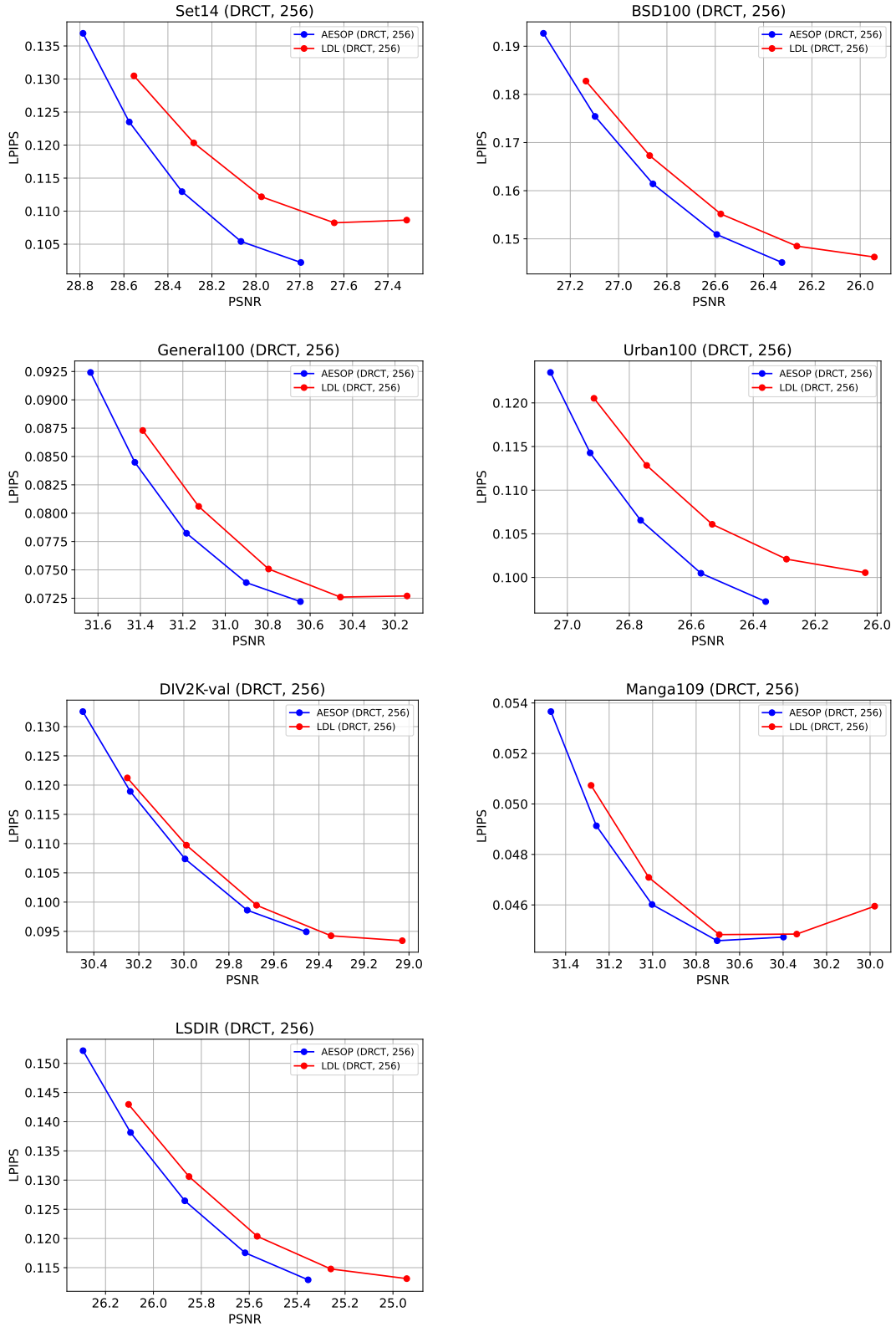


Figure 14. The perception-distortion trade-off curve between AESOP and baseline methods on top of the DRCT [18] backbone. The training HR patch size is 256. AESOP often fails to improve the performance on the Manga109 dataset.

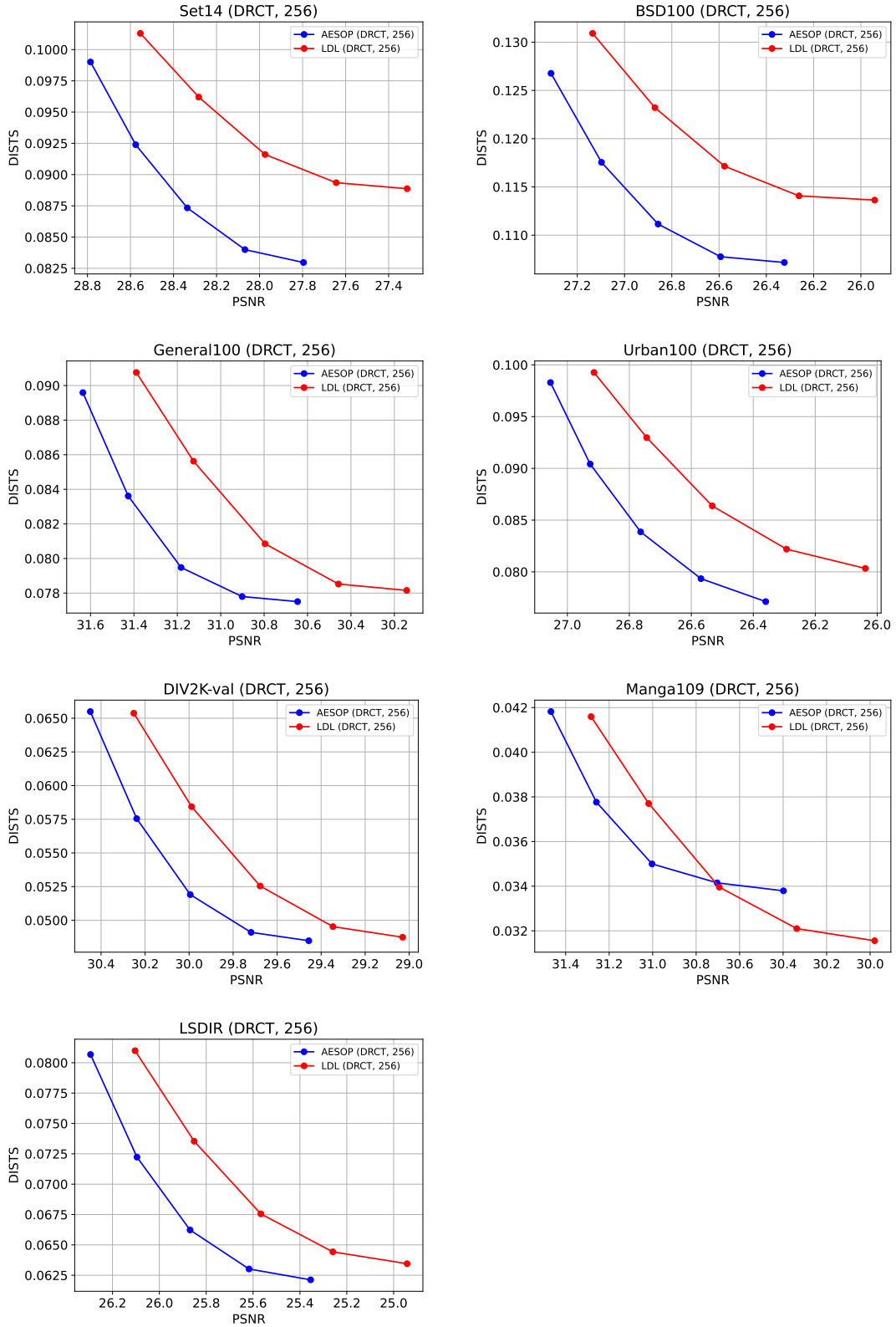


Figure 15. The perception-distortion trade-off curve between AESOP and baseline methods on top of the DRCT [18] backbone. The training HR patch size is 256. AESOP often fails to improve the performance on the Manga109 dataset.

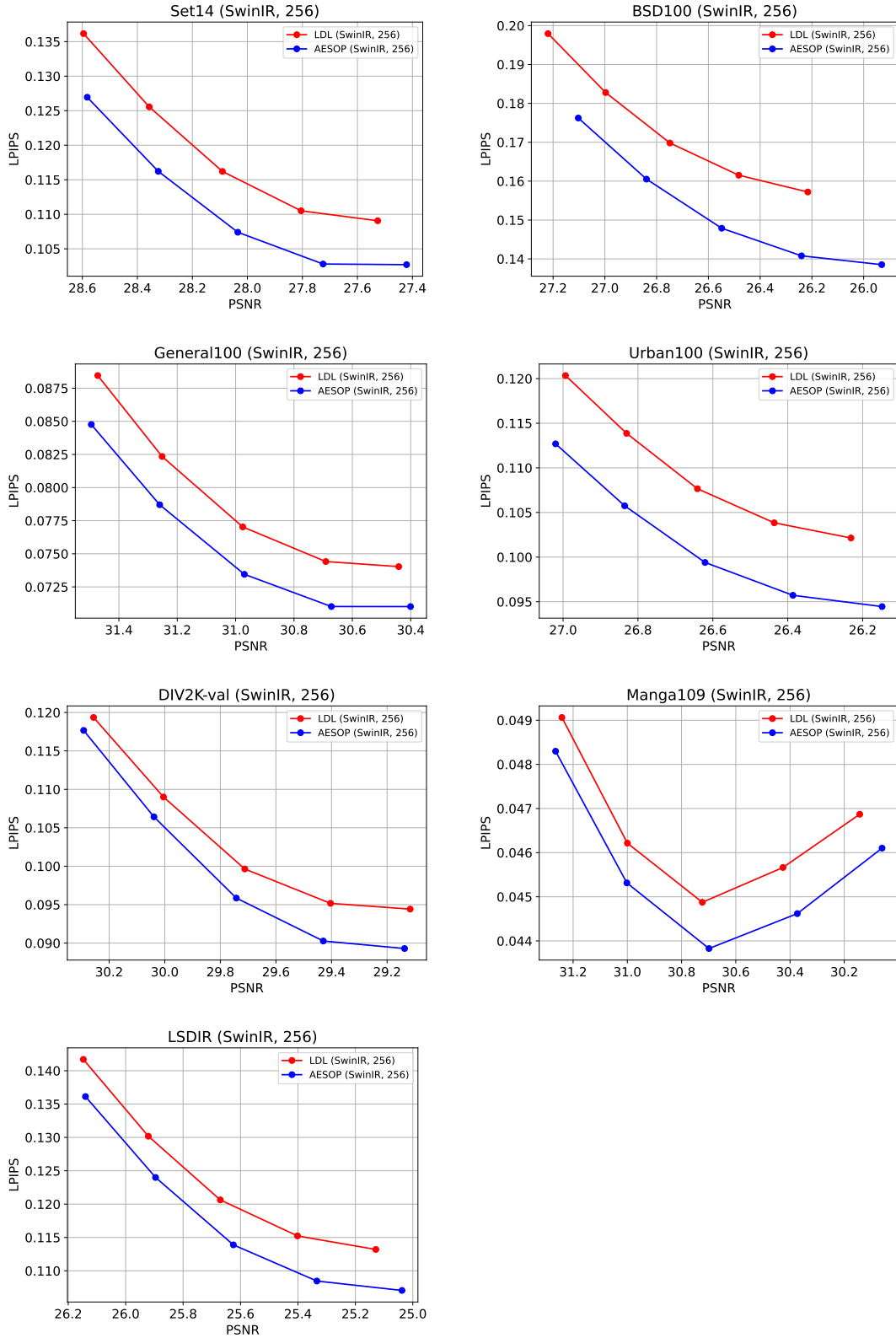


Figure 16. The perception-distortion trade-off curve between AESOP and baseline methods on top of the SwinIR [36] backbone. The training HR patch size is 256. AESOP often fails to improve the performance on the Manga109 dataset.

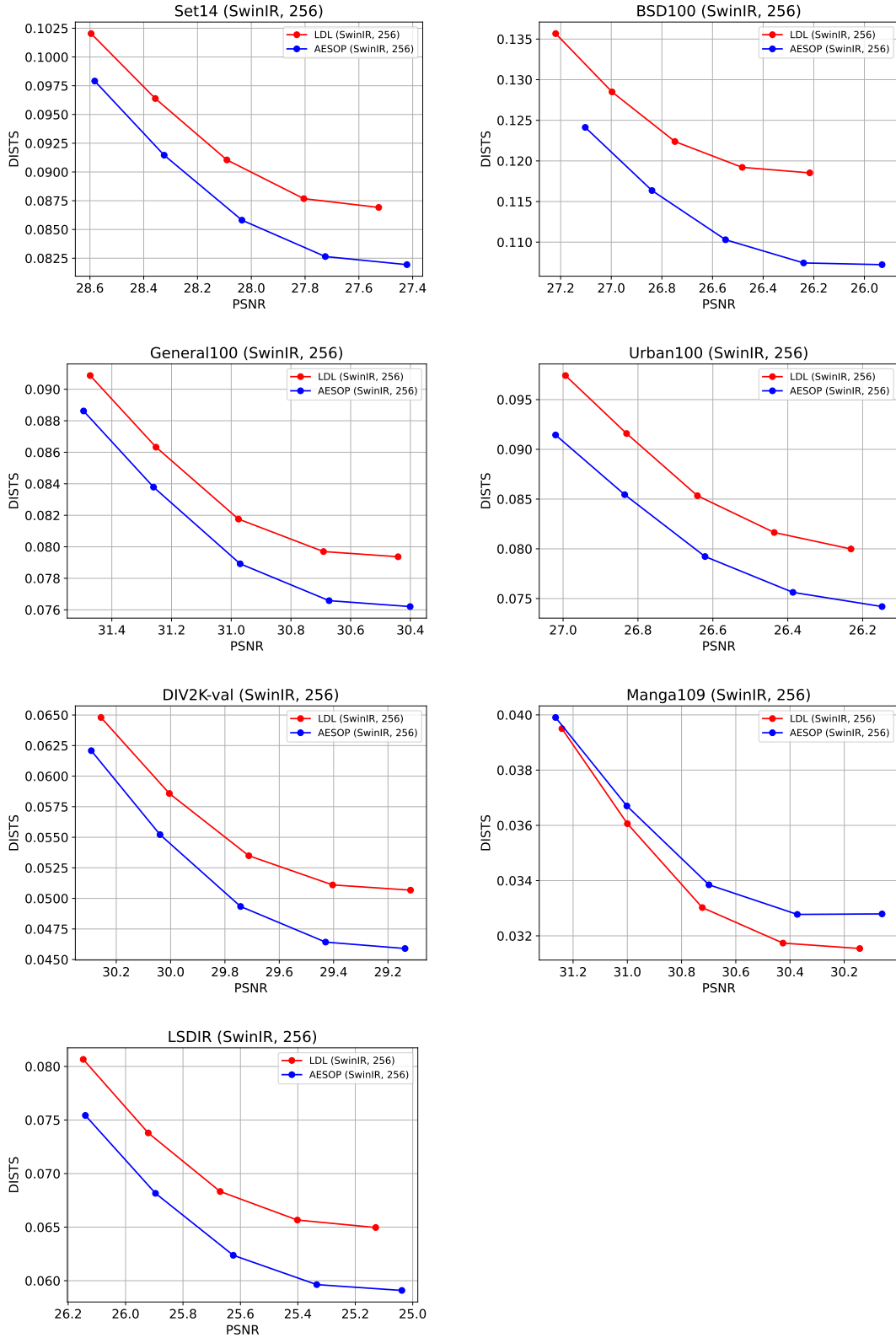


Figure 17. The perception-distortion trade-off curve between AESOP and baseline methods on top of the SwinIR [36] backbone. The training HR patch size is 256. AESOP often fails to improve the performance on the Manga109 dataset.

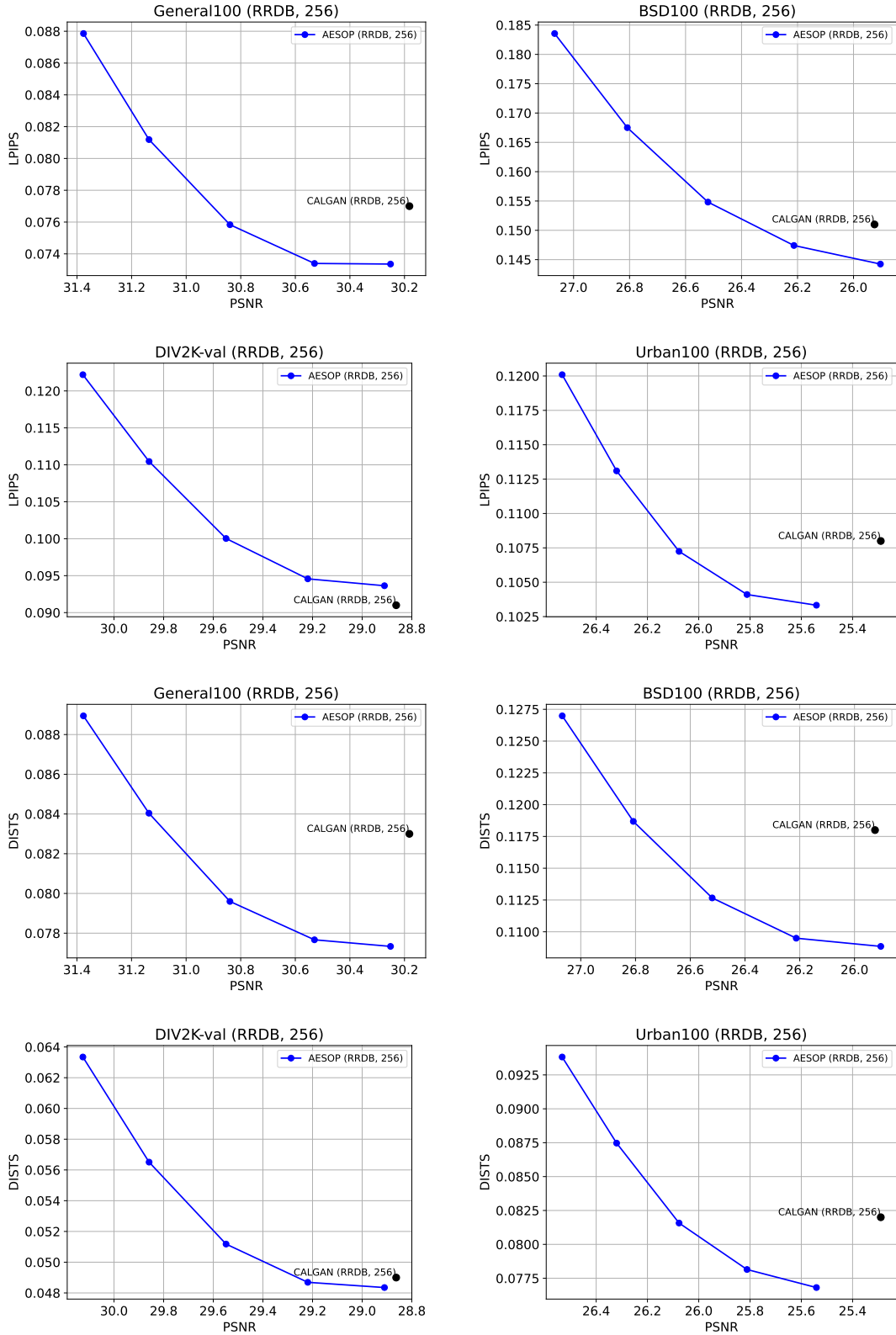


Figure 18. The perception-distortion trade-off curve between AESOP and baseline methods on top of the RRDB [54] backbone. The training HR patch size is 256. AESOP mostly outperforms CALGAN [48] even without the MoE-discriminator.

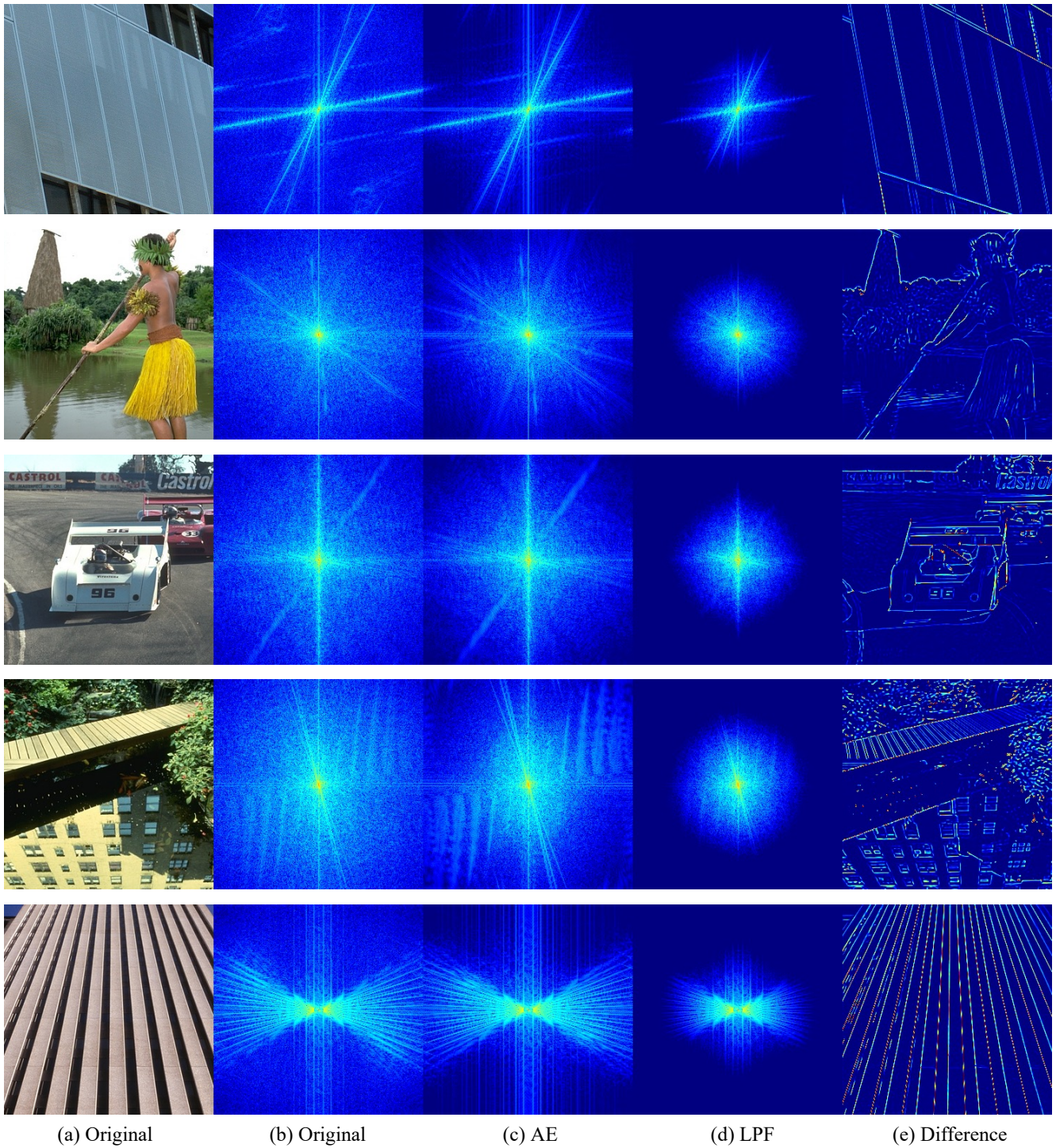


Figure 19. Visual comparison between Auto-Encoding and low-pass filtering. (a) Original image. (b) Original image in spectral domain. (c) Auto-Encoded image. (d) Low-pass filtered image. (e) Absolute difference between the Auto-Encoded image and the low-pass filtered image. **Electronic viewer recommended.**

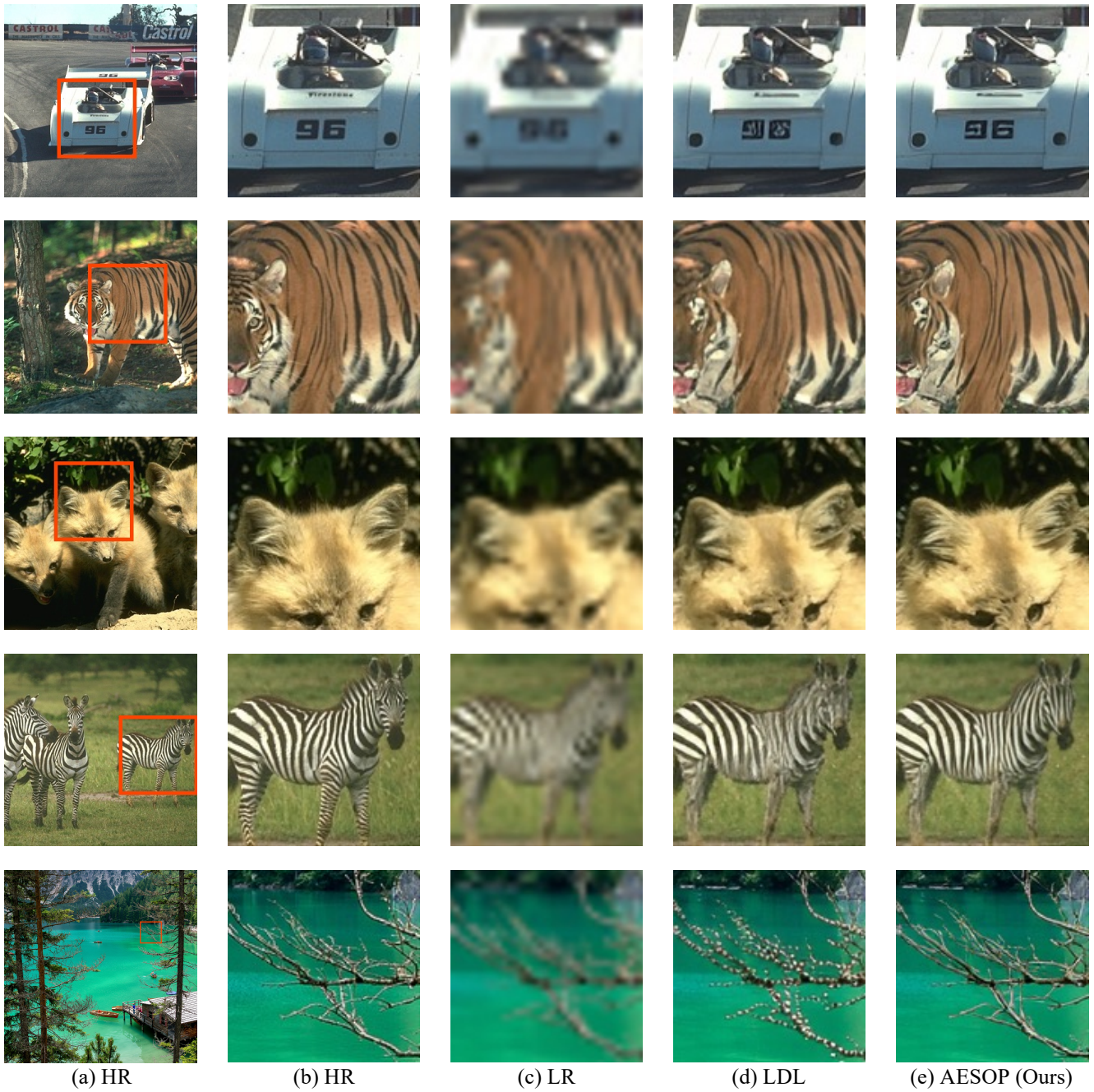


Figure 20. Visualization of AESOP (ours) and the baseline method for the bicubic $\times 4$ SR task with SwinIR backbone. AESOP can generate fine-grained textures with a lower level of visual artifacts. **Zoom in for best view.**

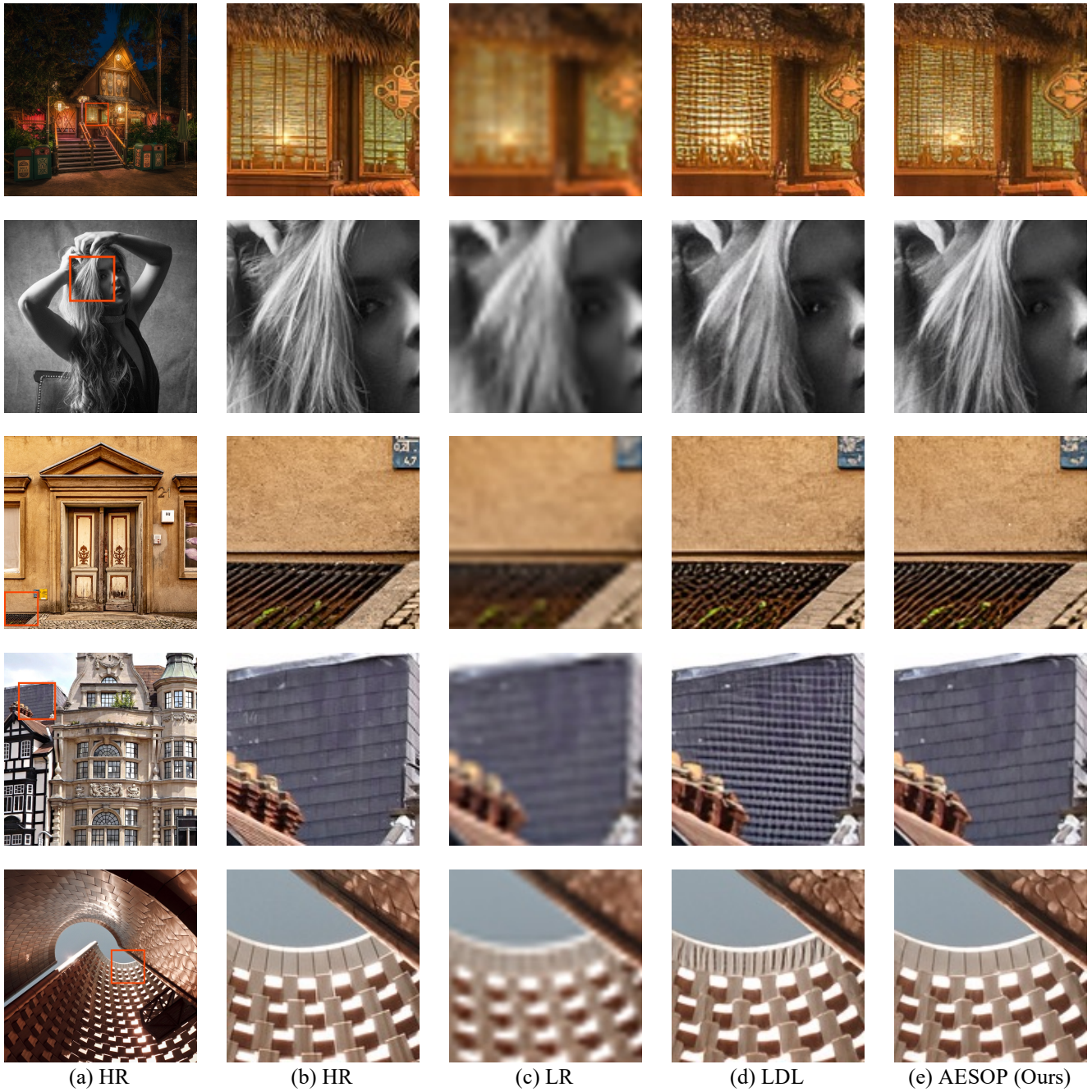


Figure 21. Visualization of AESOP (ours) and the baseline method for the bicubic $\times 4$ SR task with SwinIR backbone. AESOP can generate fine-grained textures with a lower level of visual artifacts. **Zoom in for best view.**

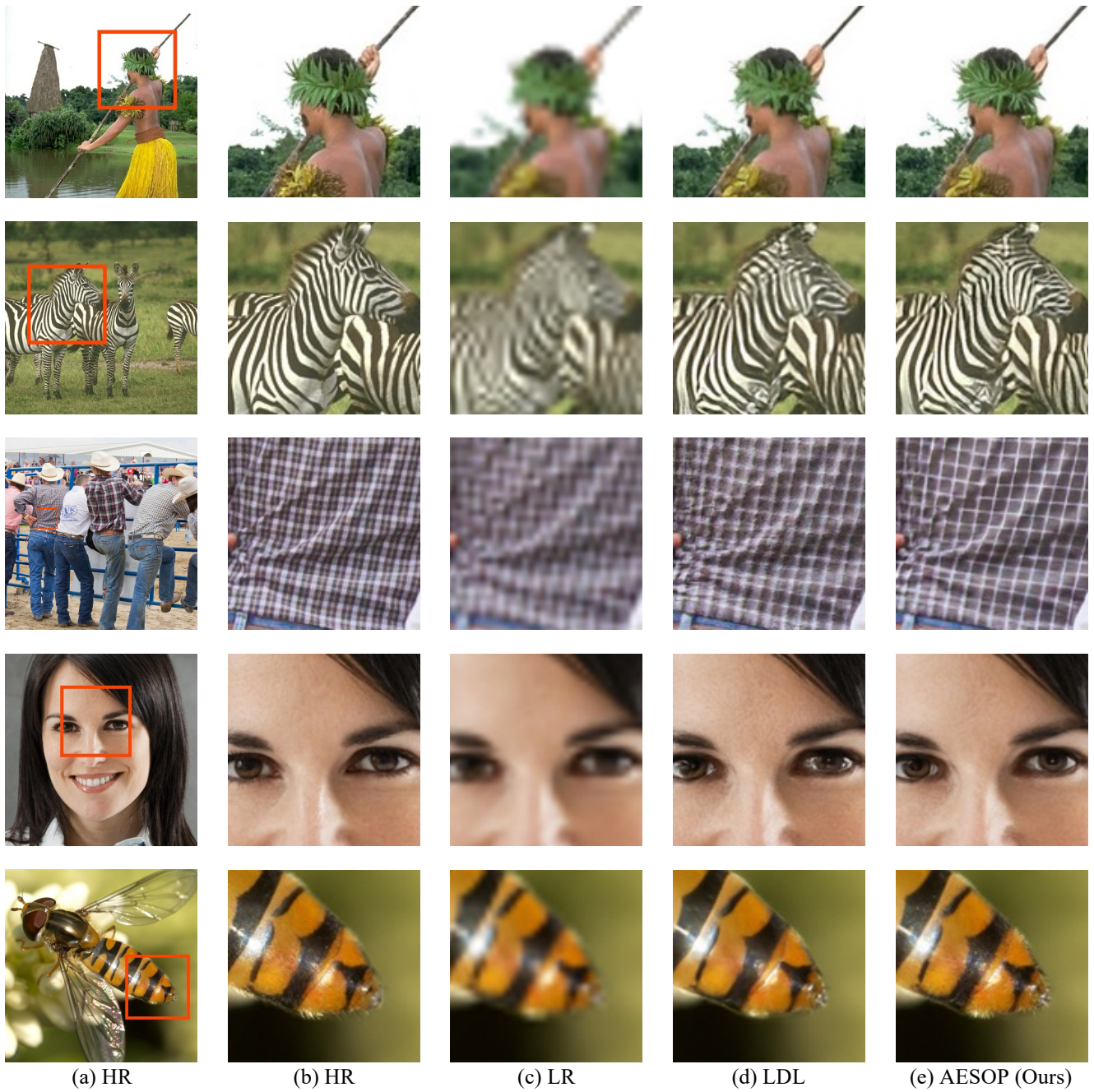


Figure 22. Visualization of AESOP (ours) and the baseline method for the bicubic $\times 4$ SR task with RRDB backbone. AESOP can generate fine-grained textures with a lower level of visual artifacts. **Zoom in for best view.**

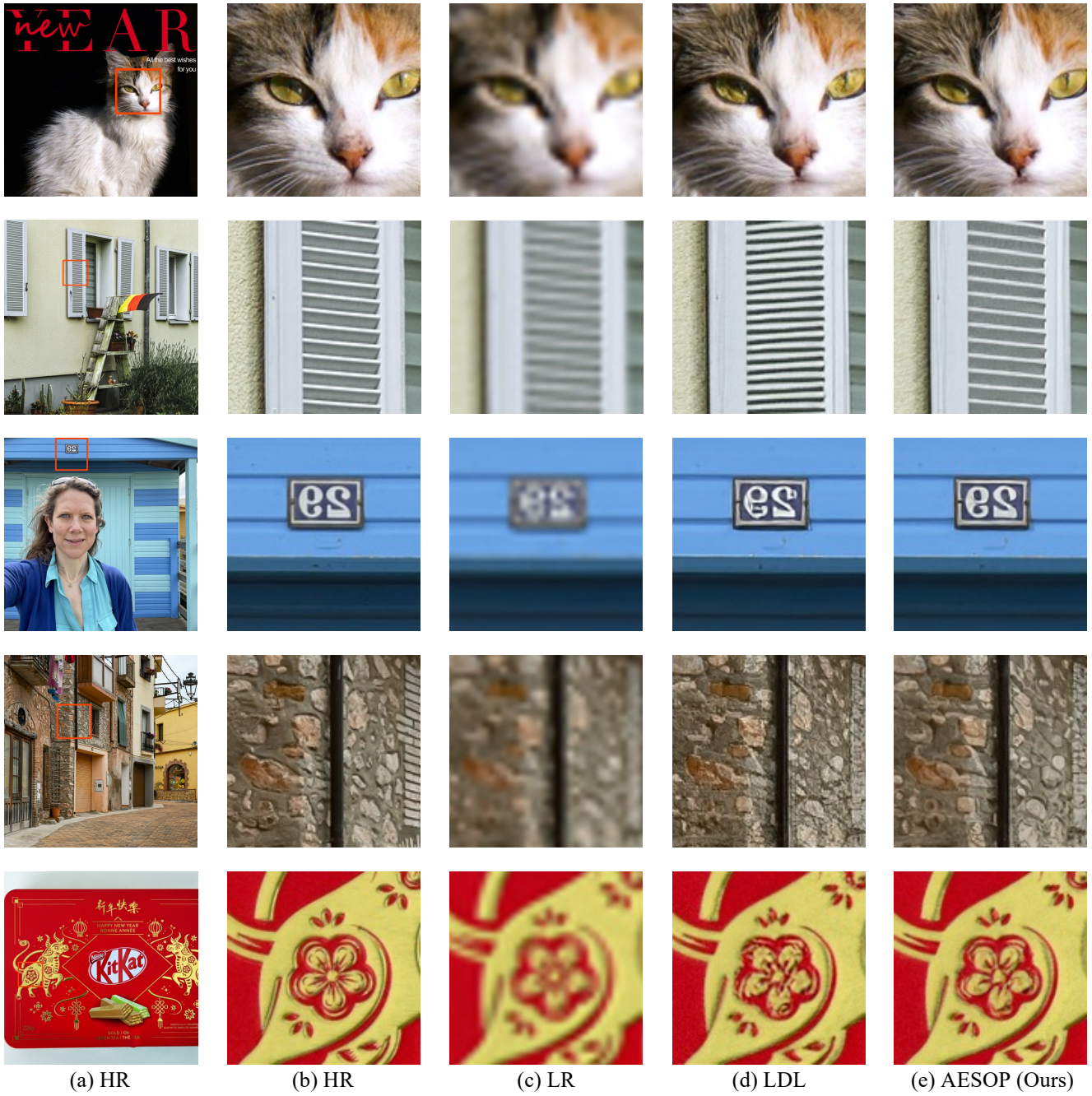


Figure 23. Visualization of AESOP (ours) and the baseline method for the bicubic $\times 4$ SR task with RRDB backbone. AESOP can generate fine-grained textures with a lower level of visual artifacts. **Zoom in for best view.**